J. Fluid Mech. (1982), *vol.* 117, *pp.* 343–377
Printed in Great Britain

Ageostrophic instability of ocean currents

By R. W. GRIFFITHS, PETER D. KILLWORTH
Department of Applied Mathematics and Theoretical Physics,
Silver Street, Cambridge CB3 9EW, England

AND MELVIN E. STERN
Graduate School of Oceanography, University of Rhode Island,
Kingston, RI 02881, U.S.A.

(Received 9 April 1981 and in revised form 17 September 1981)

We investigate the stability of gravity currents, in a rotating system, that are infinitely long and uniform in the direction of flow and for which the current depth vanishes on both sides of the flow. Thus, owing to the role of the Earth's rotation in restraining horizontal motions, the currents are bounded on both sides by free streamlines, or sharp density fronts. A model is used in which only one layer of fluid is dynamically important, with a second layer being infinitely deep and passive. The analysis includes the influence of vanishing layer depth and large inertial effects near the edges of the current, and shows that such currents are always unstable to linearized perturbations (except possibly in very special cases), even when there is no extremum (or gradient) in the potential vorticity profile. Hence the established Rayleigh condition for instability in quasi-geostrophic models, where inertial effects are assumed to be vanishingly small relative to Coriolis effects, does not apply. The instability does not depend upon the vorticity profile but instead relies upon a coupling of the two free streamlines. The waves permit the release of both kinetic and potential energy from the mean flow. They can have rapid growth rates, the *e*-folding time for waves on a current with zero potential vorticity, for example, being close to one-half of a rotation period. Though they are not discussed here, there are other unstable solutions to this same model when the potential vorticity varies monotonically across the stream, verifying that flows involving a sharp density front are much more likely to be unstable than flows with a small ratio of inertial to Coriolis forces.

Experiments with a current of buoyant fluid at the free surface of a lower layer are described, and the observations are compared with the computed mode of maximum growth rate for a flow with a uniform potential vorticity. The current is observed to be always unstable, but, contrary to the predicted behaviour of the one-layer coupled mode, the dominant length scale of growing disturbances is independent of current width. On the other hand, the structure of the observed disturbances does vary: when the current is sufficiently narrow compared with the Rossby deformation radius (and the lower layer is deep) disturbances have the structure predicted by our one-layer model. The flow then breaks up into a chain of anticyclonic eddies. When the current is wide, unstable waves appear to grow independently on each edge of the current and, at large amplitude, form both anticyclonic and cyclonic eddies in the two-layer fluid. This behaviour is attributed to another unstable mode.

1. Introduction

There have been many studies of the stability of stratified shear flows in a rotating fluid. Apart from Kelvin–Helmholtz instabilities, most studies have concentrated upon quasi-geostrophic models, in which inertial forces are small compared with Coriolis forces. These studies reveal two fundamental types of instabilities. The first of these takes place in a one-layer fluid. The resulting (barotropic) instability is driven by the horizontal shear of the basic flow, and requires an extremum in the profile of potential vorticity (i.e. absolute vorticity divided by depth). Although potential energy may be released by the instability, it is necessary that kinetic energy of the mean flow be released. The second type of instability takes place in a two-layer fluid (or, of course, a continuously stratified one). This instability, usually called baroclinic instability (cf. Pedlosky 1964), can occur without the release of mean kinetic energy but does require the release of mean potential energy that was stored in the density field. Again, a necessary condition for instability is that the gradient of potential vorticity changes sign somewhere within the fluid.

Models in which inertial forces are assumed to be much smaller than the Coriolis forces are appropriate for large-scale motions in the ocean and atmosphere, but do not provide a good description of many smaller-scale motions, such as the instabilities of density fronts in the ocean, where inertial forces can be comparable with Coriolis forces. By a 'front' we refer to the situation where a density surface intersects an upper or a lower boundary (such as the ocean surface or bottom). For this situation the conservation of potential vorticity by fluid columns aligned parallel to the axis of rotation, along with the vanishing layer depth, suggests that the fluid vorticity near the front may be comparable to the background (planetary) vorticity. Motions will then be strongly influenced by inertial forces. However, there have been very few studies (Orlanski 1968) of instabilities at density fronts because of the complexity of including the ageostrophic terms.

In this paper we want to study the situation in which the same density surface has two intersections with the same boundary (i.e. there are two fronts present). Such a situation occurs whenever buoyant water forms a narrow current at the ocean surface (away from coastal boundaries) or when dense water flows in a narrow stream over the ocean bottom under the influence of buoyancy forces. One such case is the flow of cold, dense Norwegian Sea water through the Denmark Strait and along the sloping bottom south of the strait (Worthington 1969; Mann 1969; Smith 1976). Coriolis forces are able to inhibit any slumping of the buoyant fluid in the direction perpendicular to the direction of flow and, at the same time, the presence of a cross-stream bottom slope prevents the current from curving to its right. We show here that the presence of two free streamlines, at the intersections of the density interface with the bottom on each side of the current, gives rise to another mechanism for instability. This mechanism operates even when only one layer of fluid (the current itself) is present, and instability does not depend critically upon the details of the potential vorticity profile.

Because we are particularly interested in the possibility that a *single* layer of fluid can be unstable, we consider a current flowing beneath a deep second layer which is stationary and passive. We show that a long rectilinear current bounded by two free streamlines and adjacent to a sloping (or horizontal) boundary is (almost) always unstable. Normal-mode perturbations with finite downstream wavelengths lead to the

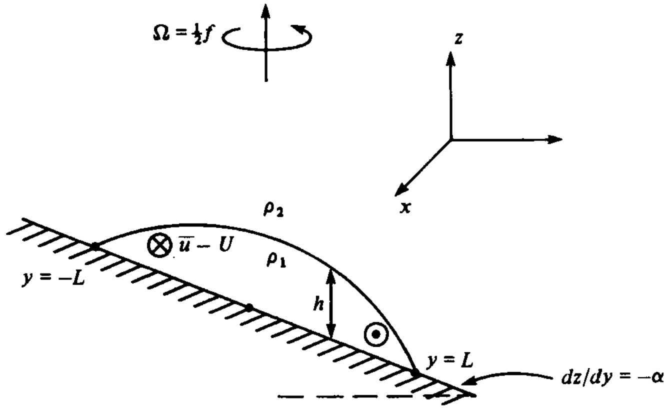

FIGURE 1. The configuration for the one-layer problem considered in this paper.

exponential growth of a combination of meandering and varicose modes.† This combination leads to release of kinetic and potential energy from the original flow. For a current with zero potential vorticity, the wavelength with maximum growth rate is predicted to be 7·9 times the deformation radius based on the maximum depth of the current, and the maximum growth rate gives an *e*-folding time of 0·57 rotation periods.

For a general vorticity distribution, it is shown that instability will always occur for sufficiently long waves whether or not the traditional Rayleigh criterion is satisfied, provided only that the undisturbed relative vorticity does not vanish at points where the flow velocity is equal to the phase velocity of growing disturbances. This kind of instability relies upon a coupling between the two edges of the current. It is therefore likely to continue to contribute to the energy release from sufficiently narrow currents when there are two layers of finite depth and where baroclinic two-layer instability may be important. As a particularly useful example (and one that may give a reasonable description of oceanic and laboratory currents – at least up to the single-layer assumption) we next consider flows with a finite but uniform potential vorticity and describe the exact numerical solution of the eigenvalue problem. In this case the radius of deformation and the current width are independent length scales. When all lengths are non-dimensionalized by the deformation radius we find that the downstream length scale of the most rapidly growing disturbance increases, while its growth rate decreases, with increasing current width.

The very unstable nature of a current with two free streamlines is demonstrated by laboratory experiments. A narrow current of buoyant fluid was produced at the free surface of a deep lower layer by floating a layer of fresh water on top of a salt solution between two axisymmetric cylindrical walls in a rotating system. When the walls were withdrawn, gravitational collapse produced a narrow annular flow with approximately uniform potential vorticity. Coupled disturbances, with a structure that was very similar to that predicted, appeared on the two fronts when the initial half-width of the current was less than twice the initial Rossby radius. The flow rapidly developed into

---

† It can also be shown that in the limit of very large downstream length scales variations of current width will give rise to a purely meandering instability. This meandering mode will grow linearly with time (Griffiths 1980).

a chain of anticyclonic eddies. The preferred downstream length scale of disturbance was 7·4 ± 1·3 times the radius of deformation for the state of geostrophic balance and was independent of current width. For narrow currents the observed length scale and structure of the instabilities can be explained by the present theory, but the model does not explain the instability that is observed when the current is wide. In that case a second mode of instability appeared to occur on each independent density front. This second mode may well require an active second layer, or else it may be the manifestation of another unstable solution to the equations for a single-layer fluid. This other unstable solution occurs on each front independently and will be discussed in another paper.

2. The stability problem

Governing equations

We consider the configuration in figure 1, in which a fluid of uniform density ρ_2 flows beneath an infinite fluid of density $\rho_1 < \rho_2$, against a uniformly sloping bottom whose (constant) gradient in the y-direction is $-\alpha$. The undisturbed flow is taken to be parallel to the x-axis. Assuming no flow in the upper layer, and that α is small enough for the hydrostatic assumption to hold, the momentum and continuity equations are

$$u_t + uu_x + vu_y - fv = -g'h_x, \tag{2.1}$$

$$v_t + uv_x + vv_y + f(u-U) = -g'h_y, \tag{2.2}$$

$$h_t + (uh)_x + (vh)_y = 0, \tag{2.3}$$

where (u,v) are the (x,y)-components of velocity, t represents time, f is the Coriolis parameter and $g' = g(\rho_2-\rho_1)/\rho_2$ is the reduced gravity. The velocity U, given by

$$U = g'\alpha f^{-1}, \tag{2.4}$$

is the constant x-component of flow induced by the sloping bottom and will often play the role of a mean advecting current. Equations (2.1)–(2.3) imply that the potential vorticity

$$P = \frac{f+v_x-u_y}{h} \tag{2.5}$$

is conserved by fluid columns. Hence, if the potential vorticity at any time is uniform throughout the flow, we may write

$$\frac{f+v_x-u_y}{h} = \frac{f}{H_0}, \tag{2.6}$$

where H_0 would be the uniform depth of the fluid when the relative vorticity is zero.

Let H be a typical depth of the undisturbed current (which, in examples, will often be the maximum depth and will occur at $y = 0$). The flow is then characterized by the radius of deformation $(g'H)^{\frac{1}{2}}f^{-1}$ and the time scale f^{-1}. Because we will be interested in downstream (x) variations with some – usually large – length scale λ, say, we define a dimensionless wavenumber

$$\epsilon = 2\pi(g'H)^{\frac{1}{2}}/f\lambda.$$

Convenient non-dimensional variables are then defined by

$$\left.\begin{aligned} x &= x^*\epsilon^{-1}(g'H)^{\frac{1}{2}}f^{-1}, \quad y = y^*(g'H)^{\frac{1}{2}}f^{-1}, \quad (u, U) = (u^*, U^*)(g'H)^{\frac{1}{2}}, \\ v &= v^*\epsilon(g'H)^{\frac{1}{2}}, \quad t = t^*\epsilon^{-1}f^{-1}, \quad h = h^*H, \end{aligned}\right\} \tag{2.7}$$

and, in the case of uniform potential vorticity, $H_0 = H\mathscr{H}$. Here the starred quantities are nondimensional. Dropping asterisks, (2.1) and (2.2) become

$$u_t + v(u_y - 1) = -(h + \tfrac{1}{2}u^2)_x, \tag{2.8}$$

$$\epsilon^2 v_t + u(\epsilon^2 v_x + 1) - U = -(h + \tfrac{1}{2}\epsilon^2 v^2)_y, \tag{2.9}$$

while the continuity equation (2.3) retains its original form. In the special case of flow with uniform potential vorticity, (2.6) becomes

$$u_y - \epsilon^2 v_x = 1 - \frac{h}{\mathscr{H}}. \tag{2.10}$$

The undisturbed flow

The undisturbed flow is taken as the steady solution of (2.8), (2.9), (2.3) with $v \equiv 0$. Then (2.9) reduces to the geostrophic relation

$$\bar{u} = U - \bar{h}_y, \tag{2.11}$$

where the bars denote the basic flow whose stability is to be investigated. If the flow has a uniform potential vorticity, (2.10) gives as an additional constraint the relative vorticity

$$\bar{u}_y = 1 - \frac{\bar{h}}{\mathscr{H}}. \tag{2.12}$$

As well as the case of general $\bar{u}$, we shall consider two special cases in this paper, both involving constant potential vorticity P. (The Rayleigh criterion for instability would need P_y to change sign, so these cases would be stable by this criterion.) One configuration is that of an infinitely long current (of dimensional width W) extending from $y = -L$ to $y = L$, where $L = fW(g'H)^{\frac{1}{2}}$. The boundary conditions on (2.11), (2.12) are then $\bar{h} = 0$ at $y = \pm L$, and the solution takes the form

$$\bar{h} = \mathscr{H}\left[1 - \frac{\cosh(y/\mathscr{H}^{\frac{1}{2}})}{\cosh(L/\mathscr{H}^{\frac{1}{2}})}\right], \quad \bar{u} = U + \mathscr{H}^{\frac{1}{2}}\frac{\sinh(y/\mathscr{H}^{\frac{1}{2}})}{\cosh(L/\mathscr{H}^{\frac{1}{2}})}. \tag{2.13}$$

Thus the flow involves two length scales, L and $\mathscr{H}$. In the limit of zero potential vorticity – the second special configuration – $\mathscr{H} \to \infty$, (2.12) yields $\bar{u}_y = 1$, and (2.13) reduces to

$$\bar{h} = 1 - \tfrac{1}{2}y^2, \quad \bar{u} = U + y. \tag{2.14}$$

In this case the current width is fixed at $L = \sqrt{2}$ and the flow is described, in dimensional terms, by the single length scale H.

The perturbation equations

We impose a small perturbation of the form $(u', v', h') = (\hat{u}, \hat{v}, \hat{h})\, e^{i(x-ct)}$ on the undisturbed flow $(\bar{u}, 0, \bar{h})$. Then the momentum and continuity equations (2.8), (2.9), (2.3) give the following linearized equations for the perturbation amplitudes:

$$(\bar{u} - c)\hat{u} + (1 - \bar{u}_y)i\hat{v} = -\hat{h}, \tag{2.15}$$

$$\hat{u}+i\epsilon^2(\bar{u}-c)\hat{v} = -\frac{d\hat{h}}{dy}, \tag{2.16}$$

$$\bar{h}\hat{u}-i\frac{d}{dy}(\hat{v}\bar{h})+(\bar{u}-c)\hat{h} = 0. \tag{2.17}$$

From (2.16) it can be seen that the downstream velocity perturbation is ageostrophic at order ϵ^2. For currents with a uniform potential vorticity (2.10) gives the additional condition that

$$\frac{d\hat{u}}{dy}-i\epsilon^2\hat{v} = -\frac{\hat{h}}{\mathscr{H}}. \tag{2.18}$$

In § 3 we present a solution of (2.15), (2.17) and (2.18) for a very simple but illuminating problem – that with zero potential vorticity. In § 4 the system (2.15)–(2.17) is discussed for completely general vorticity profiles. This discussion reveals the influence, upon disturbances, of the cross-stream distribution of vorticity and of asymmetric profiles. An exact numerical solution of (2.15), (2.17) and (2.18) for uniform potential vorticity distributions is then presented in § 5, and compared with laboratory observations in § 6.

3. Flow with zero potential vorticity

Solution of the eigenvalue problem

When the potential vorticity vanishes, $\mathscr{H} \to \infty$ and $\bar{u}_y - 1 = 0$. The longitudinal momentum, continuity and potential-vorticity relations (2.15), (2.17) and (2.18) become

$$(\bar{u}-c)\hat{u}+\hat{h} = 0, \tag{3.1}$$

$$\bar{h}\hat{u}-i\frac{d}{dy}(\hat{v}\bar{h})+(\bar{u}-c)\hat{h} = 0, \tag{3.2}$$

$$\frac{d\hat{u}}{dy}-i\epsilon^2\hat{v} = 0, \tag{3.3}$$

where $\bar{h}, \bar{u}$ are given by (2.14).

Elimination of $\hat{h}$ and $\hat{v}$ from the continuity equation (3.2) yields an eigenvalue problem for the complex phase velocity c:

$$\frac{d}{dy}\left(\bar{h}\frac{d\hat{u}}{dy}\right)-\epsilon^2[\bar{h}-(\bar{u}-c)^2]\hat{u} = 0. \tag{3.4}$$

Because $\bar{h}(\pm L) = 0$, this equation has singularities at the edges of the current, and we wish to find the solution for which the eigenfunction $\hat{u}$ is regular at $y = \pm L$.† From (3.3) we see that $d\hat{u}(L)/dy$ must be finite in order that $\hat{v}$ be finite on the free streamlines. Therefore, when (3.4) is integrated across the current, we require

$$\int_{-L}^{L} [\bar{h}-(\bar{u}-c)^2]\hat{u}\,dy = 0, \tag{3.5}$$

where $L = \sqrt{2}$.

---

† This condition may also be derived more formally by the requirement that the location of vanishing depth remain a streamline.

In order to solve (3.4), (3.5), with a finite wavenumber ϵ, c and $\hat{u}$ may be expanded in the power series

$$\left.\begin{aligned} c &= c_0+\epsilon c_1+\epsilon^2 c_2+\dots, \\ \hat{u}(y) &= u_0(y)+\epsilon u_1(y)+\epsilon^2 u_2(y)+\dots, \end{aligned}\right\} \tag{3.6}$$

where the amplitude is normalized by requiring

$$\hat{u}(0) = 1. \tag{3.7}$$

Substitution of the expansions (3.6) into (3.4), and requiring that du_0/dy be finite at $y = \pm L$, where $\bar{h} = 0$, shows that

$$\frac{du_0}{dy} = 0. \tag{3.8}$$

Hence the leading-order downstream velocity perturbation is independent of y. From (3.7) we set $u_0 = 1$ and require that $u_1(0) = u_2(0) = \dots = 0$. The eigenvalue c_0 is given by (3.5), in which the leading-order terms imply

$$u_0 \int_{-L}^{L} [\bar{h}-(\bar{u}-c_0)^2]\,dy = 0.$$

This is a quadratic equation for c_0 which, with $\bar{h}$ and $\bar{u}$ given by (2.14) and $L = \sqrt{2}$, can only be satisfied by

$$c_0 = U. \tag{3.9}$$

Thus normal modes are stable in the limit $\epsilon \rightarrow 0$, and are advected downstream at speed U.

The terms of order ϵ obtained from (3.4) imply that $du_1/dy = 0$, and, in order to satisfy (3.7), this requires $u_1 = 0$. Equating the terms of order ϵ^2 obtained from (3.4) yields an equation for the eigenfunction u_2:

$$\frac{d}{dy}\left(\bar{h}\frac{du_2}{dy}\right) = \bar{h}-\tilde{u}^2,$$

where

$$\tilde{u} = \bar{u}-U \tag{3.10}$$

is the current velocity relative to its mean velocity U. By again applying the conditions that du_2/dy be finite at $\bar{h} = 0$ and $u_2(0) = 0$, we find the ageostrophic perturbation $u_2 = \frac{1}{2}y^2$. The condition (3.5) gives

$$2Lc_1^2-\int_{-L}^{L} u_2(\bar{h}-\tilde{u}^2)\,dy = 0,$$

which yields the pure imaginary eigenvalues

$$c_1 = \pm 2i/\sqrt{15}. \tag{3.11}$$

The positive root describes exponentially growing modes that are advected downstream at speed U. Disturbances with large but finite wavelengths are therefore unstable, even though the Rayleigh condition is not satisfied.

When the calculation is continued to higher orders in ϵ a pattern emerges, with even-numbered eigenvalues being zero (apart from c_0) and the rest imaginary. However, the power-series expansion reveals that the growth $\epsilon|c|$ reaches a maximum at a wavenumber only slightly less than unity, where the series converges slowly. In

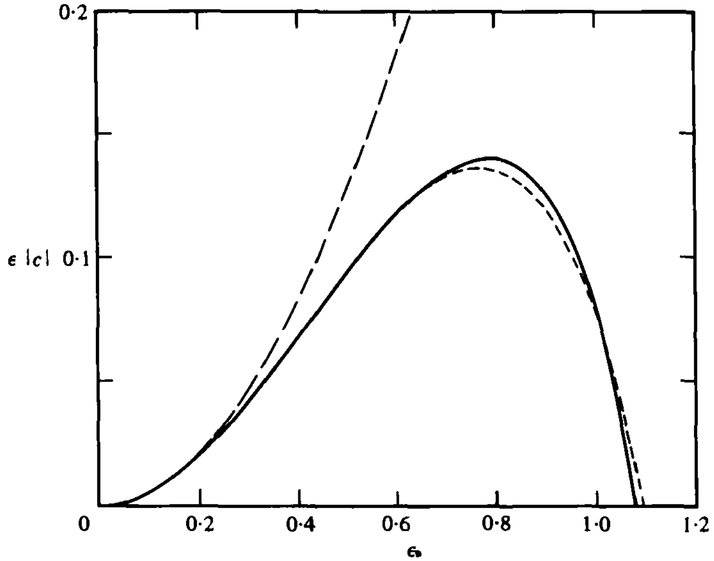

FIGURE 2. Growth rate of normal modes with wavenumber ϵ on a current with zero potential vorticity: ——, exact numerical results; – – –, first-order growth rate $\epsilon^2 c_1$ given by the wavenumber expansion; - - - - -, Padé approximation based on terms up to $O(\epsilon^{12})$ in the expansion.

order to investigate disturbances with $\epsilon \sim 1$, it was necessary to solve (3.1)–(3.3) numerically, using the Taylor system (Norman 1972). The solution was obtained by integrating from $y = L-\gamma$, where $\gamma = 10^{-4}$, with initial conditions obtained from an expansion of (3.1)–(3.3) near $\bar{h} = 0$. The solution at $y = 0$ was found. The equation was then solved again, beginning at $y = -L+\gamma$ and integrating to $y = 0$. The solutions for $\hat{u}$ were matched at $y = 0$ by scaling the solution from $y = L-\gamma$; c was then adjusted iteratively to match $\hat{u}_y$ (to an accuracy of 10^{-6}). Only imaginary eigenvalues c were found and, at $\epsilon \leqslant 1$, these are identical with those calculated using the expansion (3.6).

On figure 2 the computed dimensionless growth rate $\epsilon|c|$ is plotted as a function of the wavenumber (solid line). This numerical result is almost identical to the curve (dashed line) that is obtained from the power-series expansion (3.6), which is here extrapolated to $\epsilon > 1$ by taking the Padé approximation based on the first six nonzero terms. The growth rate achieves its maximum value at $\epsilon = 0{\cdot}80$, which corresponds to a wavelength that is 7·9 times the Rossby radius. Wavenumbers greater than $\epsilon = 1{\cdot}1$ yield only real eigenvalues and so are stable.

The eigenfunctions

Substitution of the individual functions $u_0, u_2, u_3, \ldots$ into the longitudinal momentum equation (3.1) and the vorticity equation (3.3) yields the depth and cross-stream velocity perturbations respectively, for successive orders in ϵ. Since the amplitude of each perturbation quantity (u', v', h') has the downstream dependence e^{ix} (neglecting the uniform advection velocity U), we write $(u'_0, u'_1, u'_2, \ldots) = (u_0, u_1, u_2, \ldots)\,e^{ix}$, and similarly for v' and h'. Then the real parts of the eigenfunctions of lower order in ϵ are

$$u'_0 = \cos x, \quad v'_0 = y \sin x, \quad h'_0 = -y\cos x, \tag{3.12}$$

$$v'_1 = \frac{-4}{\sqrt{15}}\cos x, \quad h'_1 = \frac{-2}{\sqrt{15}}\sin x.$$

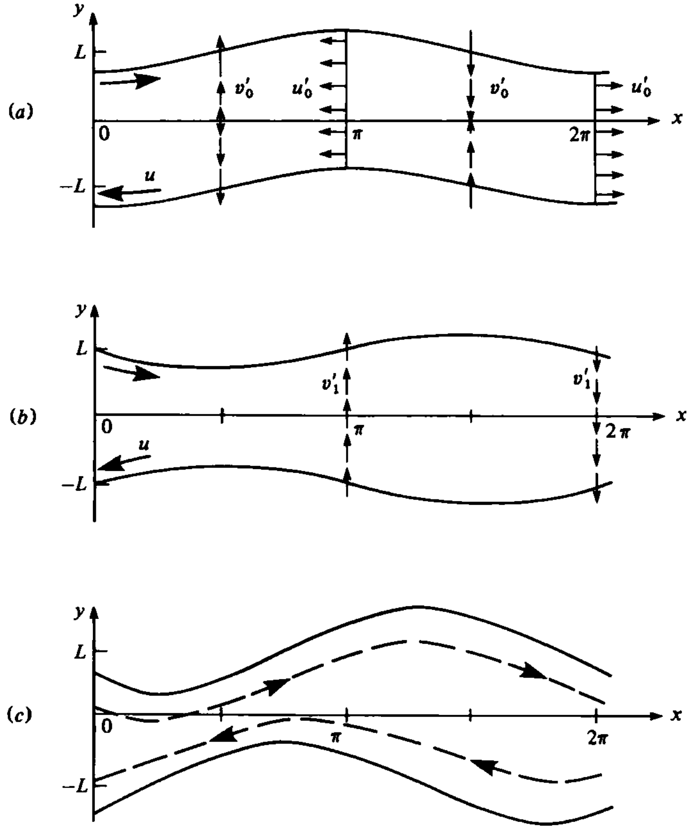

FIGURE 3. The structure of the zeroth-order eigenfunctions: (*a*) the first-order eigenfunctions; (*b*) (from (3.16)) and the combination of these two modes; (*c*) for ϵ of order one and a flow with zero potential vorticity. The undisturbed flow $\bar{u}$ is linear with y.

The nature of the zeroth-order eigenfunctions is sketched in figure 3(*a*). Because both the cross-stream velocity v' and the undisturbed longitudinal flow $\bar{u}$ are antisymmetric in y, the zeroth-order perturbation corresponds to a meandering of the stream. The corresponding depth perturbation is linear with y, so that the total depth profile $\bar{h}+h'_0$ remains symmetric and parabolic about the *local* midpoint of the current.

The first-order cross-stream velocity v'_1 is independent of position across the stream, but, because $\bar{u} = y$, it corresponds to variations in the current width, as sketched in figure 3(*b*). This perturbation has an amplitude whose phase is $\frac{1}{2}\pi$ radians ahead of v'_0. The depth perturbation h'_1 is also independent of y, and therefore tends to maintain the symmetry about the midpoint $y = 0$. As a result of the form of h'_1, the depth increases uniformly at the widest section of the current and decreases at the narrowest section.

Higher-order eigenfunctions (such as v'_2 and v'_3) have structures similar to those already described, but tend to concentrate the amplitude of perturbations nearer the two free streamlines. When the perturbations sketched in figures 3(*a*, *b*) are superimposed, noting the comparable amplitudes in (3.12) and assuming $\epsilon \sim 1$, the structure of the flow becomes that sketched in figure 3(*c*). There is still a uniform reduction of the current depth at $x = \frac{1}{2}\pi$ and a uniform increase at $x = \frac{3}{2}\pi$. When such a disturbance

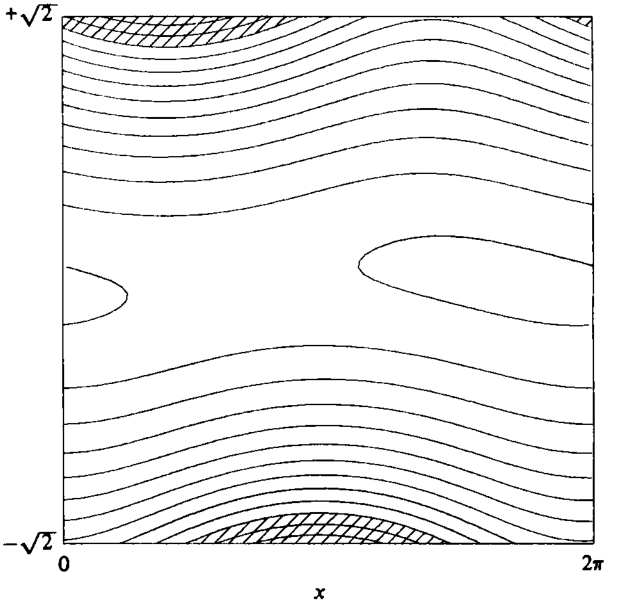

FIGURE 4. Equispaced contours of the total depth $\bar{h}+h'$ from the numerical solution for zero potential vorticity, for $\epsilon = 0{\cdot}8$ and a depth perturbation of maximum amplitude 0·28 (chosen for clarity). Regions of negative $\bar{h}+h'$ are hatched.

reaches sufficiently large amplitudes it is likely that regions of closed circulation will develop within the deeper, broader parts of the stream, and such regions will be centred about the midpoint of the flow. Figure 4 shows a plot of the contours of constant h (the total depth of the current) for the numerical solution at $\epsilon = 0{\cdot}8$. The meandering and variations of width are visible, along with a phase difference of $\frac{1}{2}\pi$ radians between the two edges of the flow. The widest sections of the current are also deepest, even deeper than the mid-point of the undisturbed flow.

Energetics

The source of energy for the growing disturbances may be determined from the structure of the depth and velocity perturbations. In order to calculate the energy changes we consider small perturbations (u', v', h') to (2.8), (2.9), (2.3), where we revert here to a general mean flow. Taking $\bar{h}u'$ times (2.8), $\bar{h}v'$ times (2.9), h' times (2.3), and adding yields the local energy equation

$$\frac{\partial E}{\partial t} + \bar{h}\bar{u}_y\langle u'v'\rangle + \{\bar{h}\langle h'v'\rangle\}_y = 0, \tag{3.13}$$

where the angle brackets denote an average in the x-direction and

$$E = \tfrac{1}{2}\langle \bar{h}(u'^2+\epsilon^2 v'^2)+h'^2\rangle \tag{3.14}$$

is a convenient measure of the energy of the perturbations (kinetic plus potential). As is well-known, interpretation of the local terms in (3.13) as kinetic and potential energy transfers is dangerous. To avoid this, we integrate (3.13) to give

$$\frac{d}{dt}\int_{-L}^{L} E\,dy = -\int_{-L}^{L} \bar{h}\bar{u}_y\langle u'v'\rangle\,dy, \tag{3.15}$$

which shows that growing perturbations draw energy from the kinetic energy of the mean flow. However, at the end of § 4 we shall show that potential energy is also released.

For the case of zero potential vorticity the Reynolds stress term $\langle u'v'\rangle$ is evaluated from (3.12) as

$$\langle u'v'\rangle = \frac{-2}{\sqrt{15}}\epsilon + O(\epsilon^2), \tag{3.16}$$

so that, as $\bar{h}\bar{u}_y$ is positive in (3.15), the perturbations induce a positive Reynolds stress which transports momentum across the stream. The superposition of meandering and varicose modes with a phase difference of $\frac{1}{2}\pi$ therefore removes kinetic energy from the mean flow. In general, though, it is not yet obvious that the right-hand side of (3.15) need be positive (and the flow unstable) for an arbitrary mean velocity profile. This is the subject of § 4, where it is shown that indeed there must always be unstable perturbations to any mean flow with two free streamlines.

4. The case of arbitrary mean profile

Formulation of the problem

We again consider a current such as that discussed in § 2. This time, however, no restrictions are placed on the depth profile save that $\bar{h} = 0$ at $y = \pm L$. The perturbation equations (2.15)–(2.17) are to be satisfied, while $\bar{u}$ and $\bar{h}$ are connected by the geostrophic constraint (2.11), and we shall show that an unstable mode exists for general depth profiles $\bar{h}$.

For convenience, an integrated depth perturbation $\phi(y)$ can be defined as

$$\phi(y) \equiv \int_{-L}^{y} \hat{h}\, dy \tag{4.1}$$

$$\equiv \phi_0 + \epsilon\phi_1 + \epsilon^2\phi_2 + \epsilon^3 \log\epsilon\,\phi_3 + \epsilon^3\phi_4 + \ldots, \tag{4.1a}$$

where the wavenumber expansion (4.1*a*) also holds for c, $\hat{u}$ and $\hat{v}$, and

$$h_n = \phi_{ny} \quad (n = 0, 1, 2, \ldots). \tag{4.2}$$

The ϕ_n must satisfy some boundary conditions and, from (4.1), we have

$$\phi_n(-L) = 0, \tag{4.3}$$

where we may choose the magnitude of $\phi_y(-L)$ arbitrarily. Selecting for convenience the value $\phi_y(-L) = -\tilde{u}(-L)$, we have

$$\left.\begin{aligned} \phi_{0y}(-L) &= -\tilde{u}(-L), \\ \phi_{ny}(-L) &= 0 \quad (n > 0). \end{aligned}\right\} \tag{4.4}$$

In addition, application of the continuity equation (2.17) at $y = \pm L$ gives, since $\hat{v}$ is well behaved,

$$\bar{u}i\hat{v} + (\bar{u} - c)\phi_y = 0 \quad (y = \pm L). \tag{4.5}$$

In general the ϕ_n will have a boundary-layer structure of thickness ϵ at critical layers (where $\tilde{u} = 0$), and an inner expansion, followed by asymptotic matching across these layers, is necessary. The details of the inner expansion are not shown explicitly here, but are recorded in appendix B, which has been lodged with the editorial office of the *Journal of Fluid Mechanics*, and will be used in what follows. An alternative proof of the existence of an unstable mode, avoiding many of the boundary-layer problems, is given in appendix A. However, that approach assumes the existence of well-behaved eigenfunctions, while the expansion technique outlined in this section explicitly finds such well-behaved eigenfunctions.

The expansions of (2.15)–(2.17) may be written symbolically as

$$(\bar{u}-c_0)\,u_n+(1-\bar{u}_y)\,iv_n+\phi_{ny}+A_n=0, \tag{4.6}$$

$$u_n+B_n=-\phi_{nyy}, \tag{4.7}$$

$$\bar{h}u_n-(\bar{h}iv_n)_y+(\bar{u}-c_0)\,\phi_{ny}+C_n=0, \tag{4.8}$$

for $n=0,1,2,\ldots$, where A_n, B_n and C_n involve combinations of terms from previous values of n with eigenvalues up to c_n. Thus

$$iv_n=\frac{(\bar{u}-c_0)\,\phi_{nyy}-\phi_{ny}+B_n(\bar{u}-c_0)-A_n}{1-\bar{u}_y}. \tag{4.9}$$

Substitution of (4.9) into (4.8), integration from $-L$ to y, and multiplication by $(1-\bar{u}_y)/\bar{h}$ gives, remembering that $\bar{h}(-L)=0$,

$$(\bar{u}-c_0)\,\phi_{nyy}-\bar{u}_y\phi_{ny}+\frac{c_0(1-\bar{u}_y)}{\bar{h}}\,\phi_n=-\frac{(1-\bar{u}_y)}{\bar{h}}\int_{-L}^{y}(\bar{h}B_n-C_n)\,dy-B_n(\bar{u}-c_0)+A_n. \tag{4.10}$$

Equations (4.9) and (4.10), with boundary conditions given by (4.4) and the expansion of (4.5), form an eigenvalue problem for each c_n. One particular solution, which couples the two free streamlines together, was isolated in § 3 for the special case of zero potential vorticity, and we now examine the corresponding solution for the general case. We show that, except under very special conditions, the mode is always unstable.

Solution up to order ϵ^2

To leading order, $A_0=B_0=C_0=0$, and, from (4.10), and (4.9), ϕ_0 and v_0 satisfy

$$(\bar{u}-c_0)\,\phi_{0yy}-\bar{u}_y\phi_{0y}+\frac{(c_0-U)\,(1-\bar{u}_y)}{\bar{h}}\,\phi_0=0, \tag{4.11}$$

$$iv_0=\frac{(\bar{u}-c_0)\,\phi_{0yy}-\phi_{0y}}{1-\bar{u}_y}. \tag{4.12}$$

The set (4.11), (4.4) and (4.5) pose an eigenvalue problem for c_0 which may have many solutions; no indication has been found of whether or not c_0 can be complex. However, we choose here to examine a *specific* solution to (4.11) in which c_0 is real, and show that to next order c is complex. We choose the solution

$$c_0=U,\quad \phi_0=\bar{h},\quad iv_0=\bar{u},\quad u_0=\bar{u}_y,\quad h_0=U-\bar{u}=-\tilde{u}, \tag{4.13}$$

so that, to leading order, the disturbance is simply propagated downstream at speed U. We see that, in general, u_0 and h_0 are real, while v_0 is imaginary, implying that u' and h' have phases which are $\frac{1}{2}\pi$ ahead of v'.

The $O(\epsilon)$ terms have $A_1 = -c_1 u_0$, $B_1 = 0$ (i.e. the along-stream flow remains geostrophic), and $C_1 = -c_1 \phi_{0y}$. Then (4.10) becomes

$$\tilde{u}\phi_{1yy} - \overline{u}_y \phi_{1y} + c_1 = 0, \tag{4.14}$$

and (4.4) gives the conditions $\phi_1 = \phi_{1y} = 0$ at $y = -L$, while the condition (4.5) gives no information to this order. Now (4.14) has two independent solutions, one with ϕ_{1y} proportional to $\tilde{u}$, and one with

$$\phi_{1y} = -c_1 \tilde{u} \int^y \frac{dy}{\tilde{u}^2}. \tag{4.15}$$

Consideration of (2.11) shows that $\tilde{u}$ must vanish at least once in the interval $(-L, L)$. The places where $\tilde{u}$ vanishes are the critical layers for this solution. We shall treat the case of one such layer (at $y = y_c$), but the extension to several layers is immediate. We shall also assume that $\overline{u}_{yc}$ (we denote values at the critical layer with a suffix c) is non-zero. (In the extreme case of $\tilde{u}$ vanishing quadratically, rather than linearly, at a critical layer, it can be shown that the solution is stable. Physically, there is stability if the vorticity $\overline{u}_y$ vanishes when $\tilde{u}$ vanishes.)

The solution (4.15) is well-behaved as $\tilde{u}$ approaches zero only if $\overline{u}_{yyc}$ is zero (as would be the case for all symmetric depth distributions, for example); otherwise the solution contains logarithmically growing terms. In either case, a matching across the critical layer is necessary. We therefore write

$$\phi_1^- = -c_1 \int_{-L}^{y} \tilde{u}(\eta)\, d\eta \int_{-L}^{\eta} \frac{d\xi}{[\tilde{u}(\xi)]^2} \quad (y < y_c), \tag{4.16}$$

$$\phi_1^+ = \beta - \alpha\overline{h} - c_1 \int_{+L}^{y} \tilde{u}(\eta)\, d\eta \int_{+L}^{\eta} \frac{d\xi}{[\tilde{u}(\xi)]^2} \quad (y > y_c), \tag{4.17}$$

where α, β are unknown constants, and the boundary conditions on (4.14) have been used to give (4.16). To match across the critical layer, we shall need the behaviour of $\phi_1^\pm$ near $y = y_c$. Writing $\eta = y - y_c$, we have

$$\begin{aligned}\phi_1^- \sim \phi_{1c}^- + \frac{c_1}{\overline{u}_{yc}}\eta + \frac{c_1 \overline{u}_{yyc}}{2\overline{u}_{yc}^2}\eta^2 (\log\eta - \tfrac{1}{2}) - \tfrac{1}{2} c_1 \overline{u}_{yc}\eta^2 \bigg\{ \int_{-L}^{y_c - \delta} \frac{dy}{\tilde{u}^2} - \frac{1}{\delta \overline{u}_{yc}^2} \\ + \frac{\overline{u}_{yyc}}{\overline{u}_{yc}^2}\log(-\delta)\bigg\} + \frac{c_1 \overline{u}_{yyc}\eta^2}{\overline{u}_{yc}^2} \quad (\eta < 0),\end{aligned} \tag{4.18}$$

$$\begin{aligned}\phi_1^+ \sim \phi_{1c}^+ + \frac{c_1}{\overline{u}_{yc}}\eta + \tfrac{1}{2}\alpha\overline{u}_{yc}\eta^2 + \frac{c_1 \overline{u}_{yyc}}{2\overline{u}_{yc}^2}\eta^2 (\log\eta - \tfrac{1}{2}) - \tfrac{1}{2} c_1 \overline{u}_{yc}\eta^2 \bigg\{ \int_{L}^{y_c + \delta} \frac{dy}{\tilde{u}^2} + \frac{1}{\delta \overline{u}_{yc}^2} \\ + \frac{\overline{u}_{yyc}}{\overline{u}_{yc}^2}\log\delta\bigg\} + \frac{c_1 \overline{u}_{yyc}}{\overline{u}_{yc}^2}\eta^2 \quad (\eta > 0),\end{aligned} \tag{4.19}$$

where $\delta > 0$ is a small positive number. The expression $\log(-\delta)$ is to be interpreted as $\log\delta \pm i\pi$, and from the inner expansion it is found that this must be

$$\log\delta - i\pi \operatorname{sgn}(\overline{u}_{yc}).$$

At $O(\epsilon^2)$ in (4.6)–(4.8), $A = -c_1 u_1 - c_2 u_0$, $B_2 = \tilde{u}^2$ and $C_2 = -c_1\phi_{1y} - c_2\phi_{0y}$. Hence the flow becomes ageostrophic at this order. Then from (4.10) ϕ_2 satisfies

$$\tilde{u}\phi_{2yy} - \overline{u}_y\phi_{2y} + \frac{1-\overline{u}_y}{\overline{h}} \int_{-L}^{y} \overline{h}\tilde{u}^2\, dy + \tilde{u}^3 - c_1\phi_{1yy} + c_2 + \frac{c_1(1-\overline{u}_y)}{\overline{h}}\phi_1 = 0, \tag{4.20}$$

together with $\phi_2 = \phi_{2y} = 0, y = -L$.

The condition (4.5) at $y = +L$ yields the same result as requiring ϕ_2 to be well-behaved in (4.20) when $\bar{h}$ vanishes, namely

$$c_1\phi_1(L) = -\int_{-L}^{L} \bar{h}\tilde{u}^2\, dy. \tag{4.21}$$

The results of the asymptotic matching are straightforward, with ϕ_1, ϕ_{1y} being continuous at $y = y_c$, the $\eta^2 \log \eta$ behaviour being handled by the inner expansion, and the well-behaved part of ϕ_{1yy} being continuous at $y = y_c$. We now match the $O(\eta^2)$ terms in the expansions (4.18), (4.19) for ϕ_1 to find the coefficient α introduced in (4.17): for $\delta \rightarrow 0$

$$\alpha = \frac{i\pi\bar{u}_{yyc}}{|\bar{u}_{yc}|^3}c_1 - c_1\left\{\left(\int_{-L}^{y_c-\delta} + \int_{y_c+\delta}^{L}\right)\frac{dy}{\tilde{u}^2} - \frac{2}{\delta\bar{u}_{yc}^2}\right\}. \tag{4.22}$$

The term in brackets is well known to be the Hadamard 'finite part' of the (divergent) integral of $\tilde{u}^{-2}$, and is a well-defined negative quantity. Its value is that of a naive integration of $\tilde{u}^{-2}$ from $-L$ to $+L$, cavalierly ignoring the singularity at y_c, and simply substituting the end values $+L$ into the integration.

Having an expression for the constant α, we can now evaluate $\phi_1(L)$ and then make use of (4.21) to find the eigenvalue c_1. First note that ϕ_1 is continuous at y_c, so that

$$\begin{aligned}\phi_1(L) &= \left\{\int_{L}^{y_c-\delta} + \int_{y_c-\delta}^{y_c+\delta} + \int_{y_c+\delta}^{L}\right\}\phi_{1y}\, dy \\ &= -c_1\int_{-L}^{y_c-\delta} dy\, \tilde{u}\int_{-L}^{y}\frac{d\eta}{[\tilde{u}(\eta)]^2} + O(\delta) + \int_{y_c+\delta}^{L}\alpha\tilde{u}\, dy - c_1\int_{y_c+\delta}^{L} dy\, \tilde{u}\int_{y_c+\delta}^{L}\frac{d\eta}{[\tilde{u}(\eta)]^2}.\end{aligned} \tag{4.23}$$

Using the geostrophic relation (2.11), integrating (4.23) by parts, and substituting for α from (4.22) gives, for small δ,

$$\phi_1(L) = -c_1\left\{\left(\int_{-L}^{y_c-\delta} + \int_{y_c+\delta}^{L}\right)\frac{\bar{h}}{\tilde{u}^2}\, dy - \frac{2\bar{h}_c}{\delta\bar{u}_{yc}^2}\right\} + \frac{i\pi\bar{u}_{yyc}\bar{h}_c c_1}{|\bar{u}_{yc}|^3} \tag{4.24}$$

$$= -c_1\, \mathrm{Fp}\int_{-L}^{L}\frac{\bar{h}}{\tilde{u}^2}dy + \frac{i\pi\bar{u}_{yyc}\bar{h}_c}{|\bar{u}_{yc}|^3}\, c_1, \tag{4.25}$$

where we use the notation Fp to denote the finite part of the integral. Then (4.21) gives, finally,

$$c_1^2 = \frac{\int_{-L}^{L}\bar{h}\tilde{u}^2\, dy}{\mathrm{Fp}\int_{-L}^{L}\bar{h}\tilde{u}^{-2}\, dy - i\pi\bar{u}_{yyc}\bar{h}_c/|\bar{u}_{yc}|^3}. \tag{4.26}$$

(For several critical layers, the last term in the denominator becomes a sum over all critical layers.)†

If $\bar{u}_{yyc}$, the gradient of relative vorticity at the critical layer, does not vanish, then (4.26) gives c_1^2 as complex, and so there exists a mode with $\mathscr{I}(c_1) > 0$, and there is instability. If $\bar{u}_{yyc}$ does vanish, it is easy to see that the finite part of the integral is

---

† The formula (4.26) has been confirmed by numerical integration of (2.15)–(2.17) for specific asymmetric profiles.

negative.† Hence c_1 is only imaginary and the positive root of (4.26) gives an unstable mode. We have therefore proved the existence of an unstable wave mode for all distributions of depth, except in the unusual case when $\overline{u}_{yc}$ vanishes at a critical layer. The above analysis even holds in the zero-potential-vorticity case (§ 3) despite the fact that $1-\overline{u}_y$ in (4.12) then vanishes identically. The expression (4.26) reduces to $c_1^2 = -\frac{4}{15}$ in that case, in agreement with the analysis in § 3.

Energy transfers

The energetics of currents with arbitrary velocity profiles are easily evaluated. We have (outside the critical layer, which has a negligible extra contribution) the Reynolds stress

$$\langle u'v'\rangle = \tfrac{1}{2}\mathscr{R}(u_0v_0^*)+\tfrac{1}{2}\epsilon\mathscr{R}(u_0v_1^*+u_1v_0^*)+O(\epsilon^2), \tag{4.27}$$

where the asterisk denotes complex conjugate. Using (4.13), the zeroth-order terms cancel. The first-order perturbation eigenfunction can be found from (4.18) and gives, after simplification,

$$\mathscr{R}(u_0v_1^*) = \overline{u}_y\mathscr{R}(ic_1+i\phi_{1y}), \tag{4.28a}$$

$$\mathscr{R}(u_1v_0^*) = \mathscr{R}(-i\overline{u}_y\phi_{1y}+ic_1), \tag{4.28b}$$

whence

$$\langle u'v'\rangle = -\tfrac{1}{2}\epsilon c_{1i}(1+\overline{u}_y)+O(\epsilon^2), \tag{4.29}$$

where c_{1i} is the imaginary part of c_1. Then (3.15) yields

$$\frac{d}{dt}\int_{-L}^{L}E\,dy = \tfrac{1}{2}\epsilon c_{1i}\int_{-L}^{L}\overline{h}\overline{u}_y(1-\overline{u}_y)\,dy+O(\epsilon^2) \tag{4.30}$$

and, after use of (2.11),

$$\frac{d}{dt}\int_{-L}^{L}E\,dy = \tfrac{1}{2}\epsilon c_{1i}\int_{-L}^{L}(\overline{h}\overline{u}_y^2+\overline{h}_y^2)\,dy > 0.$$

Hence the perturbation energy is indeed growing with time (as it must for exponentially growing modes).

Finally, we note that the perturbation mass (i.e. heat) transfer across-stream is given by

$$\langle v'h'\rangle = \tfrac{1}{2}\epsilon c_{1i}\tilde{u}. \tag{4.31}$$

In the problem of § 3 (and also in § 5), the sign of (4.31) is such that the mass flux is directed outwards from $y = 0$. The further significance of $\langle v'h'\rangle$ appears when we form an expression from the continuity equation (2.3) for the rate of change of mean potential energy $\frac{1}{2}\langle h\rangle^2$, where again $h = \overline{h}+h'$:

$$\frac{\partial}{\partial t}\tfrac{1}{2}\langle h\rangle^2+\overline{h}\langle v'h'\rangle_y = 0. \tag{4.32}$$

---

† This is best seen by considering the sign of ϕ_{1y} in (4.16), (4.17). If $\tilde{u}$ vanishes only once, for simplicity, $\tilde{u}$ is negative for $y < y_c$ and positive for $y > y_c$. Hence (4.15) and (4.22) show that $\phi_{1y}c_1^{-1}$ is positive for $y < y_c$ and for $y > y_c$, so that $\phi_1(L)$ is a positive multiple of c_1 in this case. Then (4.21) implies that c_1 is purely imaginary.

Then

$$\frac{d}{dt}\int_{-L}^{L} \tfrac{1}{2}\langle h\rangle^2 \, dy = -\int_{-L}^{L} \tilde{u}\langle v'h'\rangle \, dy$$
$$= -\tfrac{1}{2}\epsilon c_{11}\int_{-L}^{L} \tilde{u}^2 \, dy < 0. \tag{4.33}$$

In other words, release of mean potential energy is also necessary during the growth of the unstable mode discussed here. However, after a little algebra it may also be shown that the *total* potential energy, given by the integral of $(\frac{1}{2}\langle h\rangle^2 + \frac{1}{2}\langle h'^2\rangle)$, is invariant. Conservation of total energy (kinetic plus potential) thus implies that *total* kinetic energy is also invariant.

5. An example: currents with uniform potential vorticity

The results in § 4 can be applied to any particular distribution of vorticity. They show that (almost) all currents of the form sketched in figure 1 are unstable to a wave mode whose growth relies upon a coupling of the two free streamlines, and the general analysis gives useful physical understanding of the flow. However, the expansion about small wavenumber is not suitable for describing the most rapidly growing mode, which is that likely to be observed in laboratory experiments. We therefore present exact numerical solutions of the eigenvalue problem (2.15)–(2.17) for one particular case: that of currents with a finite and uniform potential vorticity $\mathscr{H}^{-1}$, for which the undisturbed flow is given by (2.13). The current is now also assumed to be flowing over a horizontal plane, so that the advection velocity U is zero.

For both the numerical solutions and comparison of these with experimental results it is much more convenient, when there is a uniform potential vorticity, to modify the original non-dimensionalization (2.7). By using the 'potential vorticity depth' H_0, rather than the maximum current depth H, as a depth scale, one of the two length scales L and $\mathscr{H}$ can be eliminated from (2.13). Thus we define a new dimensionless wavenumber k and a current width L_0 by

$$k = \epsilon\mathscr{H}^{\frac{1}{2}} = 2\pi\frac{(g'H_0)^{\frac{1}{2}}}{f\lambda}, \quad L_0 = \frac{L}{\mathscr{H}^{\frac{1}{2}}} = \frac{fW}{(g'H_0)^{\frac{1}{2}}}, \tag{5.1}$$

and similarly rescale current depth and velocities using H_0 instead of H in (2.7). The potential vorticity $\mathscr{H}^{-1}$ can be expressed in terms of the current width L by using the definition $\bar{h}(0) = 1$ in (2.13), whence

$$\mathscr{H}^{-1} = 1 - \frac{1}{\cosh L_0}. \tag{5.2}$$

If $L_0 \to 0$, we approach the limit of zero potential vorticity $\mathscr{H}^{-1} = 0$, while a very wide current, $L_0 \to \infty$, implies that $\mathscr{H}^{-1} \to 1$. In these new variables the undisturbed flow becomes

$$\bar{h} = 1 - \frac{\cosh y}{\cosh L_0}, \quad \tilde{u} = \frac{\sinh y}{\cosh L_0}. \tag{5.3}$$

The momentum and continuity equations (2.8), (2.9) and (2.3), as well as the perturbation equations (2.15)–(2.17), are all unchanged except that ϵ is replaced by k.

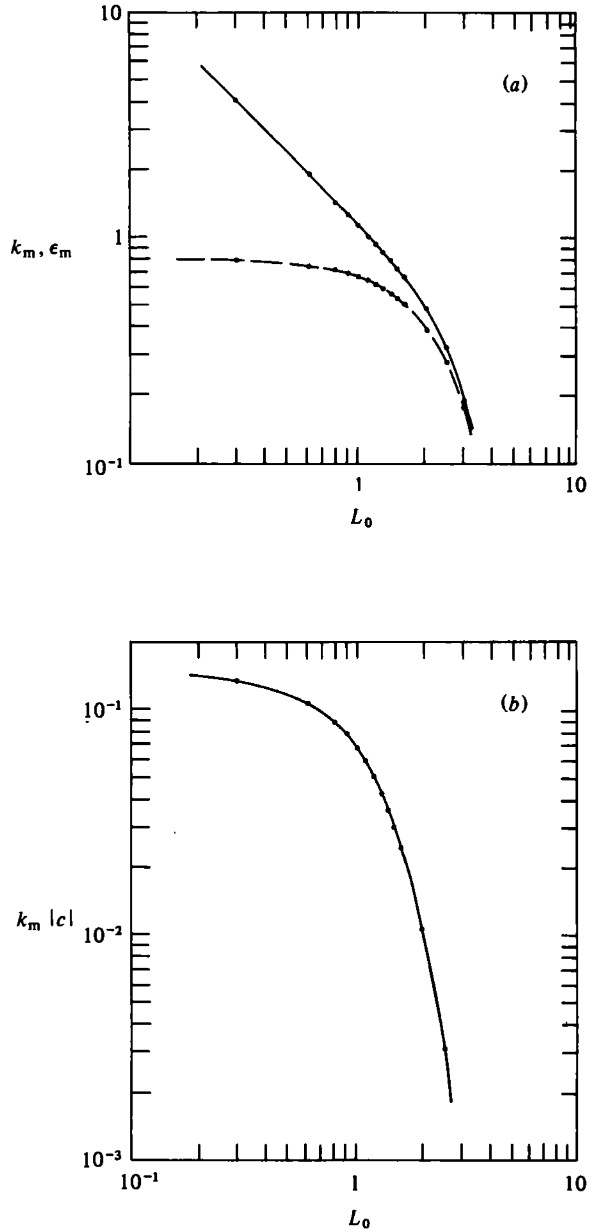

FIGURE 5. The computed wavenumber k_m (*a*) and growth rate $k_m|c|$ (*b*) for the most rapidly growing mode on a current with uniform potential vorticity, as functions of the current width $L_0 = fW/(g'H_0)^{\frac{1}{2}}$. In (*a*) the wavenumber ϵ_m, which is non-dimensionalized by the Rossby radius based on the maximum depth H, is also plotted (broken line).

Numerical solutions

The perturbation equations (2.15)–(2.17), with k replacing ϵ and with the undisturbed flow defined by (5.3), have been solved using a numerical approach similar to that described in § 3. The solution was first computed for a range of values of the wavenumber k and a number of values of the width L_0. As for the case of flow with zero potential vorticity, the eigenvalues are all found to be pure imaginary. Hence the normal modes are unstable and are again advected downstream at speed U.

For each value of L_0, the dimensionless growth rate $k|c|$ increases with increasing wavenumber at $k \ll 1$, but reaches a maximum and decreases rapidly at sufficiently large wavenumbers. The wavenumber k_m at which the maximum growth rate is achieved was found by solving the equations at successively intermediate values of k near the maximum of the growth-rate curves. Resulting values of k_m are shown on figure 5(*a*). The most rapidly growing waves are relatively long ($k_m < 1$) when the current is 'wide' ($L_0 > 1$), and they are short (with $k_m > 1$) when the current is 'narrow'. More quantitatively, k_m satisfies the relation $k_m \simeq 1{\cdot}1 L_0^{-1}$ approximately for $L_0 < 2$, but decreases much more rapidly with increasing L_0 when $L_0 > 2$. On figure 5(*a*) we have also plotted ϵ_m (broken line), which is the dimensionless wavenumber (with maximum growth rate) based upon the length scale $(g'H)^{\frac{1}{2}} f^{-1}$. The two wavenumbers are related through L_0 by combining the definition $k = \epsilon \mathscr{H}^{\frac{1}{2}}$ with (5.2). (The two are significantly different at small values of L_0, where the current depth H differs more radically from the 'potential-vorticity depth' H_0.) As $L_0 \rightarrow 0, \epsilon_m$ approaches an upper limit of $\epsilon_m \simeq 0{\cdot}8$. This limit corresponds to flow with zero potential vorticity,† and the wavenumber is the same as that found in § 3. At $L_0 \gg 1$, on the other hand, $H \rightarrow H_0$, so that ϵ_m and k_m become identical. The most rapidly growing mode then has a wavelength that is very much larger than the Rossby radius $(g'H)^{\frac{1}{2}} f^{-1}$.

On figure 5(*b*) is plotted the growth rate $k_m|c|$ of the most rapidly growing mode as a function of the current width L_0. For small values of L_0 this growth rate approaches the maximum growth rate previously computed for normal modes on a current with zero potential vorticity (see figure 2). However, the growth rate decreases exponentially when the current width is increased beyond $L_0 = 1$. At $L_0 = 2$ the growth rate $k_m|c|$ is an order of magnitude smaller than it is at $L_0 = 0{\cdot}5$, giving an e-folding time $(k_m|c|f)^{-1}$ of eight rotation periods.

The rapid decrease of growth rate with increasing current width is predicted by the wavenumber expansion of § 4. For a current of the form (5.3), the general results (4.26) for the first-order eigenvalue reduces readily to

$$c_1^2 = -\tfrac{1}{2}(\cosh L_0)^{-2}\left[1 - \tfrac{2}{3}\tanh^2 L_0 - \frac{2L_0}{\sinh 2L_0}\right]. \tag{5.4}$$

Here, c_1 is imaginary for all values of L_0, but its magnitude decreases exponentially at large L_0: $c_1 \sim \pm i(\tfrac{2}{3})^{\frac{1}{2}} \exp(-L_0)$ $(L_0 \gg 1)$. It can also be shown that there are no other long-wave solutions for the case of constant potential vorticity.

The structure of growing disturbances

Examples of computed depth and velocity perturbations for a current with uniform potential vorticity are shown in figure 6. In this case the width was $L_0 = 1$ (giving a potential vorticity $\mathscr{H}^{-1} = 0{\cdot}35$) and the amplitude $\hat{h}$ of the depth perturbation was set at 10^{-1}. Figures 6(*a*, *b*) show contours of the total depth $h + h'$ and depth perturbation h', respectively, while figure 6(*c*) shows contours of the cross-stream velocity

---

† Note that use of the wavenumber-expansion technique discussed in §§ 3 and 4 will not allow us to approach the limit of zero potential vorticity ($\mathscr{H} \rightarrow \infty$) at any finite value of ϵ, since we would require $k = \epsilon \mathscr{H}^{\frac{1}{2}} \ll 1$ (but of course this is no deterrent to a numerical solution). Thus we cannot simply let $L_0 \rightarrow 0$ (analytically) to recover the zero-potential-vorticity case.

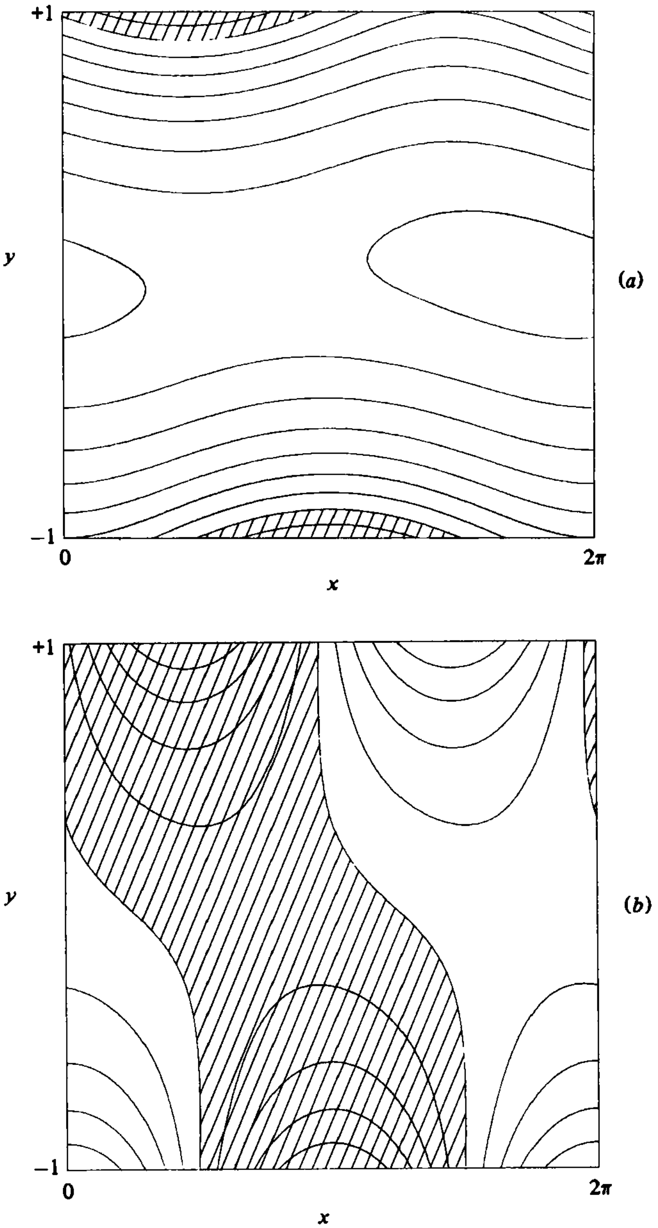

FIGURE 6 (a, b). Legend on p. 362.

perturbation v' for the same most-rapidly growing disturbance. As predicted by the wavenumber-expansion technique (§§ 3 and 4), the perturbation involves both a meandering and a longitudinal variation of current width. There is a phase difference of $\frac{1}{2}\pi$ radians between h' on the two free streamlines, and the greatest cross-stream excursions of the centre line occur at x-positions very close to where $|\partial L_0/\partial x|$ is greatest.

From figure 6 it can be seen that the depth perturbation and, similarly, the perturbation energy (as indicated by v') are confined more closely to the edges of the current

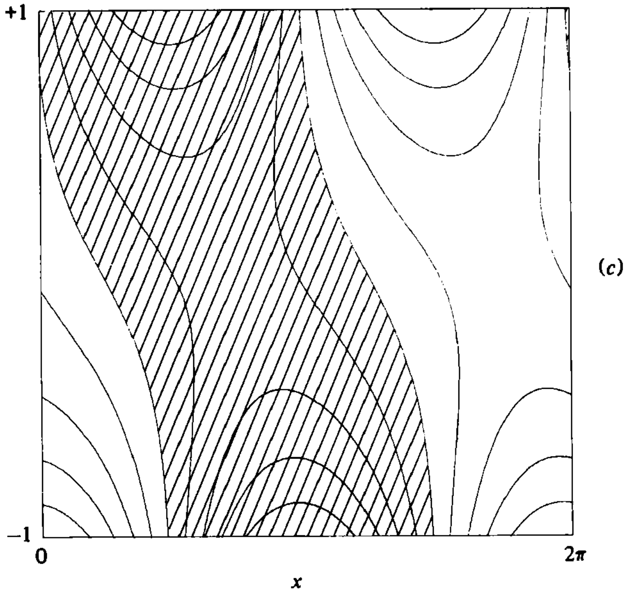

FIGURE 6. Contours of (a) the total depth $\bar{h}+h'$, (b) the depth perturbation h', and (c) the cross-stream velocity perturbation v' for the most rapidly growing mode on a current with uniform potential vorticity and $L_0 = 1$. The solution in (a) is for a depth perturbation of amplitude 0·1. Regions of negative values are hatched.

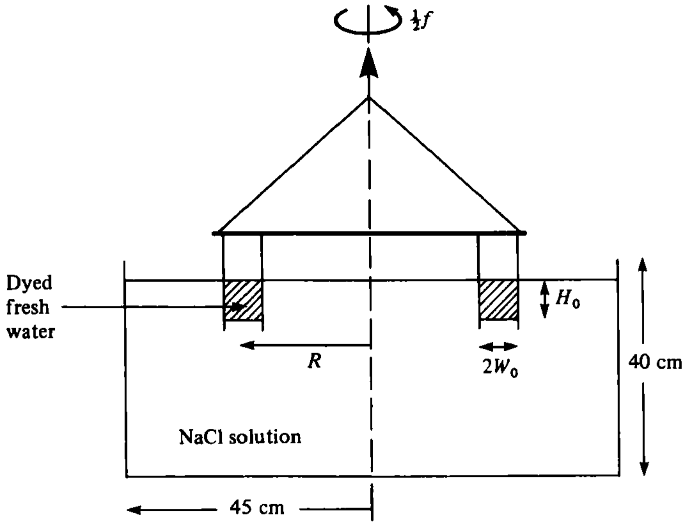

FIGURE 7. A sketch of the laboratory apparatus in vertical section. The cross-hatching indicates the upper layer of fresh, dyed water inside the annulus and the deep lower layer is a NaCl solution.

(even for $L_0 = 1$) than was the case for perturbations on currents with zero potential vorticity. From the power-series solution presented in § 4 the leading-order eigenfunctions (4.13) reduce, for constant potential vorticity, to the simple forms

$$u_0 = \frac{\cosh y}{\cosh L_0}, \quad h_0 = -iv_0 = -\frac{\sinh y}{\cosh L_0}. \tag{5.5}$$

The hyperbolic functions at this and higher orders tend to concentrate the perturbation energy into regions closer to the two free streamlines. This is where the basic flow has the greatest depth variation and a concentration of relative vorticity:

$$-d\bar{u}/dy = -\cosh y/\cosh L_0.$$

The concentration of perturbations near the fronts is much stronger for wider currents, flows for which the vorticity $\bar{u}_y$ at the centre line is much smaller and for which we know that the disturbances grow much more slowly.

Hence our restriction that the flow has a uniform potential vorticity results in a coupling between the two free streamlines that becomes very much weaker as L_0 becomes larger. On the other hand, it must be remembered that currents with more-general vorticity distributions are able to be much wider than the Rossby radius based on the fluid depth H while still having a more uniform distribution of relative vorticity, thus making larger growth rates possible for wide currents.

6. Laboratory experiments

Apparatus

Currents with an approximately uniform potential vorticity and which were bounded on each side by a well-defined density front were produced in a rotating container. In order that the flow be initially uniform along the current, an axisymmetric configuration was used. The free surface of a relatively deep lower layer of dense fluid then served as a horizontal (geopotential) surface on which the current flowed. This also greatly reduced the influence of friction below that which would be induced by a solid boundary. The depth of the lower layer of sodium chloride solution was, in most experiments, either 28 cm or 40 cm. A large annulus with a relatively narrow gap between its walls was partially immersed in the lower layer, as sketched in figure 7. The annulus was suspended from above and held concentric with the vertical axis of rotation of the container and stationary in the rotating frame of reference. Three different annuli were used. One had an inner radius of 19·8 cm and an outer radius of 23·8 cm, leaving a gap of half-width $W_0 = 2\cdot0$ cm. The others had mean radii of 20·0 cm and 21·5 cm, with half-widths $W_0 = 3\cdot9$ cm and $W_0 = 3\cdot5$ cm, respectively. The outer wall of the rotating container was at a radius of 45 cm.

After the salt solution had come to the desired rotation rate $\Omega = \frac{1}{2}f$, dyed fresh water was carefully floated onto the free surface inside the annulus to form the shallow upper layer of depth H_0 shown in figure 7. The system was then left for at least 30 min to reach solid-body rotation everywhere. The depth H_0 could be determined both by observing a vertical scale horizontally through the Perspex walls and by measuring the volume of upper layer fluid placed in the annulus. At a time $t = 0$ the annulus was carefully drawn vertically upwards and removed. The subsequent flow was made visible by the dye in the upper layer and small pellets of paper floating on the free surface. Photographs were taken with a camera mounted in the rotating reference frame and time exposures of about one-half of a rotation period were used to obtain streaks. Such streaks, as well as direct observations, revealed no motion before the annulus was withdrawn. Values of the Coriolis parameter f ranged from $0\cdot38\ \mathrm{s}^{-1}$ to $2\cdot5\ \mathrm{s}^{-1}$, while the reduced gravity g' lay in the range $0\cdot2 < g' < 12\ \mathrm{cm\ s}^{-2}$. The initial depth H_0 of the upper layer was always between 4 and 6 cm. This gave a ratio of layer

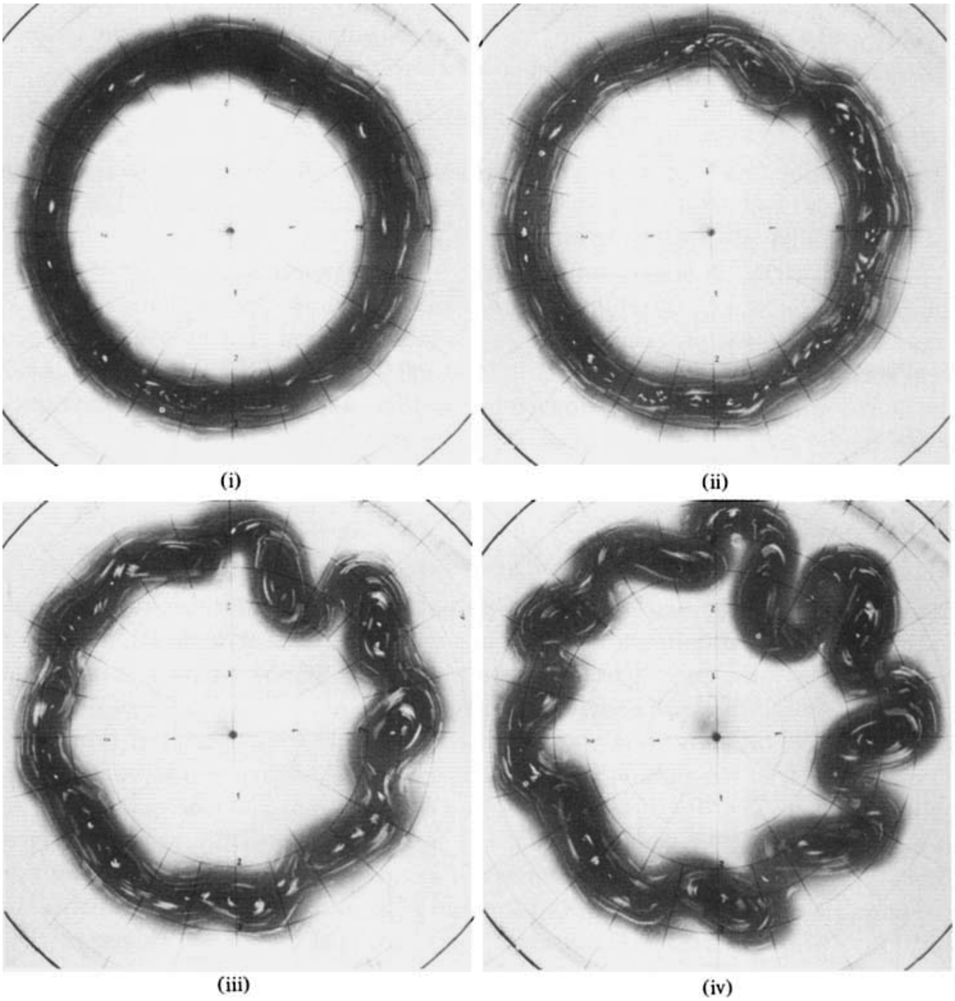

Figure 8. Streak photographs showing four stages in the evolution of a laboratory current with $W_0 = 2\cdot0$ cm, $f = 1\cdot77\ \mathrm{s}^{-1}$ and $\mathscr{L}_0 = 1\cdot18$ (4 s exposures). Times after withdrawal of the annulus are (in number of revolutions): (i) $t = 2$; (ii) 4; (iii) 6; (iv) 8. The ratio of layer depths is 0·17. Concentric circles on the bottom of the tank have a 5 cm spacing.

depths in the range 0·1–0·16 or in the range 0·16–0·2 when the lower layer was 40 cm deep or 28 cm deep, respectively. However, some experiments were also carried out with *shallow* lower layers in order to observe the influence upon the flow of the lower boundary. In these cases the initial ratio of layer depths was between 0·8 and 0·9.

Experimental observations

When the annulus was removed, the buoyant upper-layer fluid first spread radially toward and away from the axis of rotation by a distance that was measured to be close to the Rossby radius $(g'H_0)^{\frac{1}{2}}f^{-1}$. This collapse brought the flow into an approximately geostrophic balance (described by (2.11)) within a time scale of order f^{-1}. An anticyclonic (clockwise) flow is produced in the outer half of the upper layer and a cyclonic flow in the inner half, while any motion in the deep lower layer can be neglected. The axisymmetric geometry requires that both potential vorticity and angular momentum be conserved by the fluid in each layer during the collapse and that there is a balance between the buoyancy, Coriolis and centrifugal forces in the final state. The ratio of centrifugal and Coriolis accelerations is given by $\overline{u}/fr \sim (g'H_0)^{\frac{1}{2}}/fR$, where R is the radius of the annulus. For most experiments this parameter was less than 10^{-1}, but it reached 0·2 for experiments with large Rossby radii. Therefore the geostrophic basic flow assumed in the analysis in previous sections is only approximately realized.

Even before the geostrophic collapse was complete, rapidly growing billows (believed to be Kelvin–Helmholtz billows) with length scales of the order of 2 cm appeared on each edge of many of the currents. However, these disturbances also dissipated rapidly (often before the first photograph could be taken), presumably mixing some of the fluid near the fronts, and the current again became axisymmetric for a time. Later, but always within two or three revolution periods, disturbances with much larger downstream length scales appeared on the otherwise uniform flow. Subsequently, the current always broke up into a chain of eddies within five to ten revolutions.

If we assume that the deep bottom layer is stationary and that there is no mixing between the layers during the collapsing phase, then the laboratory current is described by the two dimensionless parameters $fW_0/(g'H_0)^{\frac{1}{2}}$ and W_0/H_0. In order to relate the parameters before and after the initial collapse, we write $W_0 = A/2H_0$, where A is the cross-sectional area of the current, and define

$$\mathscr{L}_0 \equiv \frac{fW_0}{(g'H_0)^{\frac{1}{2}}} = \frac{fA}{2H_0(g'H_0)^{\frac{1}{2}}}. \tag{6.1}$$

By integrating the hyperbolic depth profile (5.5), the area A can be found in terms of $L_0 = fW/(g'H_0)^{\frac{1}{2}}$ (where W is the half-width *after* collapse). Then (6.1) gives

$$\mathscr{L}_0 = L_0 - \tanh L_0. \tag{6.2}$$

Then the final width $L_0 \rightarrow 0$ when $\mathscr{L}_0 \rightarrow 0$, while $L_0 \simeq \mathscr{L}_0 + 1$ when $\mathscr{L}_0 \gg 1$.

In figure 8 are shown four stages during the evolution of a current that was formed when the initial Rossby radius was equal to the half-width W_0 of the annulus ($\mathscr{L}_0 = 1·18$). In (i) the flow is largely axisymmetric and the relative vorticity is distributed throughout the width of the current. In (ii) the streaks reveal that regions of closed anticyclonic circulation have appeared near the centre line of the current. The fronts (edges of the dyed fluid) also reveal a wavelike structure. There appears to be some meandering away from the initial centre line as well as variations in current width. Both become more obvious in (iii), where the flow appears to be qualitatively very similar to that sketched in figure 4(*c*), except that at this large amplitude there are closed circulations within the deeper sections of the current. In this case there are nine or ten waves around the annulus. In (iv), individual eddies have broken off from their neighbours and the flow become a broad region of anticyclonic eddies. These subsequently decay very slowly due to friction.

In figure 9 is shown a similar sequence in the evolution of a current for which the initial Rossby radius was $1·56W_0$ ($\mathscr{L}_0 = 0·74$). Frame (i) again shows an almost axisymmetric flow. However, small 'cat's-eye'-shaped disturbances are already visible near the centre line ($y = 0$). Only one revolution later (ii) these disturbances influence

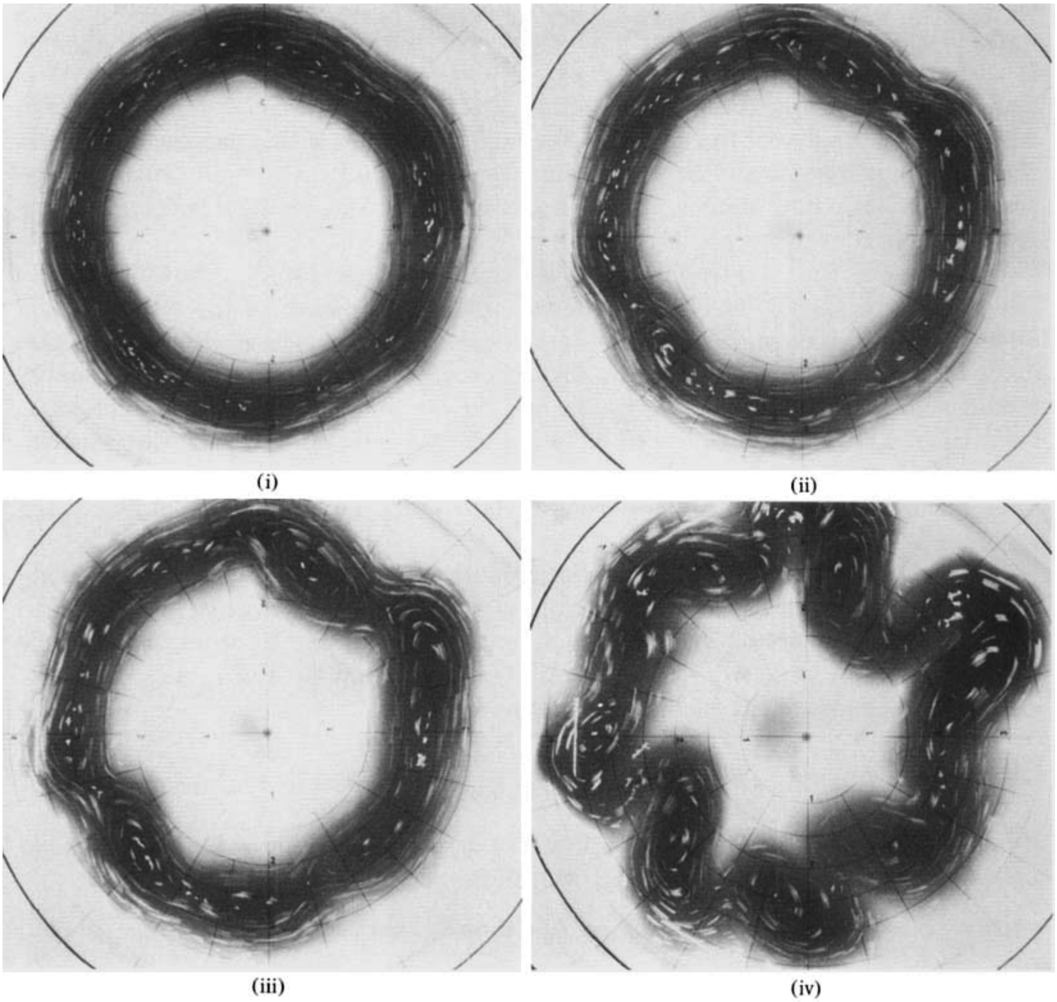
(i) (ii) (iii) (iv)

FIGURE 9. Streak photographs showing the evolution of a laboratory current with $W_0 = 2\cdot0$ cm, $f = 1\cdot11\ \mathrm{s}^{-1}$, and $\mathscr{L}_0 = 0\cdot74$ (4 s exposures). Times after withdrawal of the annulus are (in number of revolutions): (i) $t = 3$; (ii) 4; (iii) 6; (iv) 8. The ratio of layer depths is 0·17.

the whole flow. In this case there are seven waves around the annulus and both the varicose and meandering nature of the flow is visible. In (iii) and (iv) the anticyclonic eddies again develop and break up the current.

For contrast, figure 10 shows the evolution of a current that is much wider than the Rossby radius ($\mathscr{L}_0 = 4\cdot0$). As for the experiments shown in figures 8 and 9, the initial ratio of layer depths is 0·17. In this case disturbances could be seen first at the edges of the current (i) and rapidly grew in amplitude to take the form of waves that 'break' on their upstream side (ii). The two fronts then appear to behave independently. Vortices of opposite sign develop in the lower layer behind each 'breaking' crest (iii) and can lead to the formation of vortex pairs at each edge of the flow. The resulting turbulent current is shown in (iv). When the ratio of layer depths was less than 0·2 this apparently two-layer flow occurred for all currents with $\mathscr{L}_0 > 2$.

For large depth ratios, the transition between the two kinds of behaviour occurs

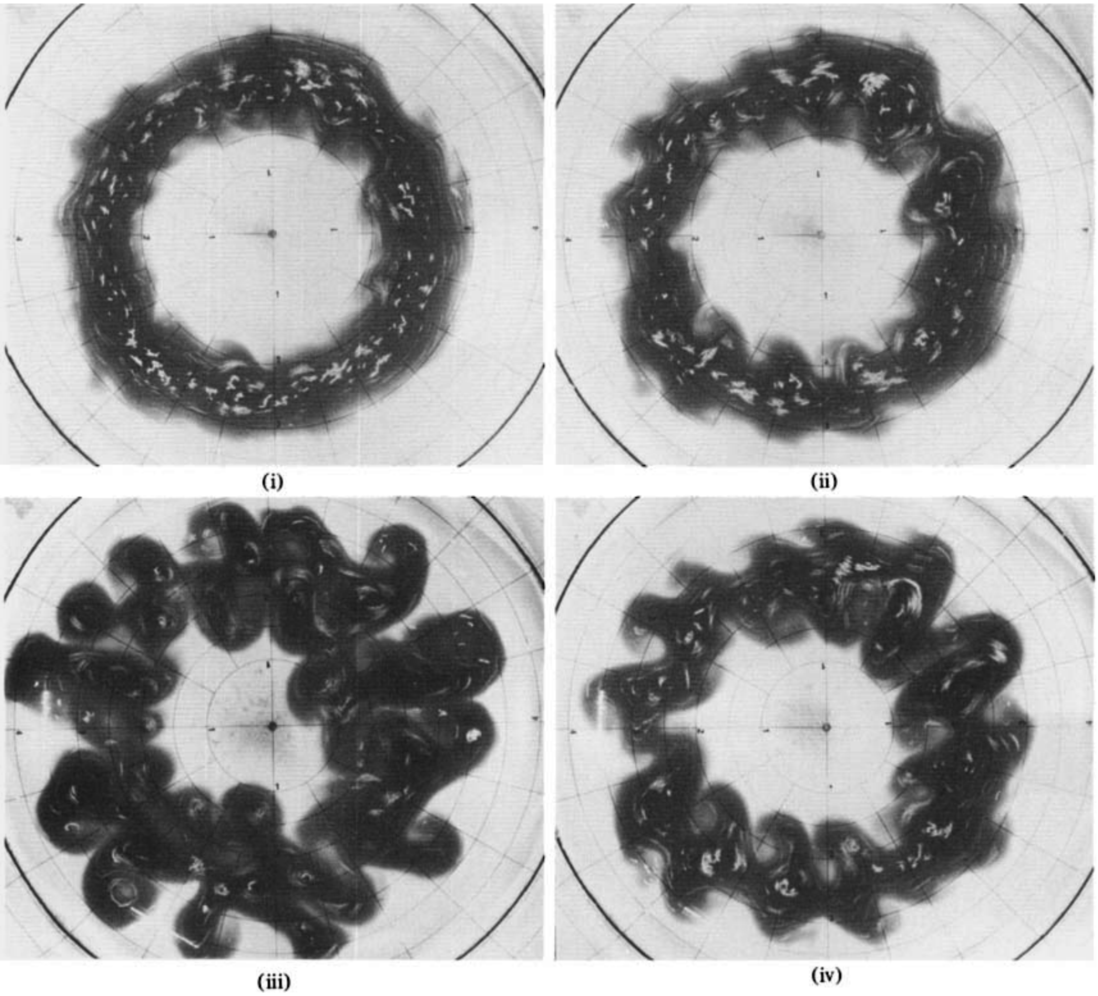

(i) (ii)

(iii) (iv)

FIGURE 10. Streak photographs showing the evolution of a laboratory current with $W_0 = 3{\cdot}9$ cm, $f = 2{\cdot}87\ \mathrm{s}^{-1}$ and $\mathscr{L}_0 = 4{\cdot}0$ (4 s exposures). Times in number of revolutions after withdrawal of the annulus are (i) $t = 3$; (ii) 4; (iii) 6; (iv) 12. The ratio of layer depths is 0·17.

near $\mathscr{L}_0 = 1$. Figure 11 shows two stages in the evolution of a current with $\mathscr{L}_0 = 1{\cdot}07$ and a ratio of layer depths 0·84. The disturbances still appear to be dominated by a coupling between the two density fronts. The waves do not 'break' and no cyclonic eddies develop in the lower layer. On the other hand, when $\mathscr{L}_0 = 3{\cdot}7$ and the depth ratio is 0·9, each edge behaves independently. This case is shown in figure 12, where the initial axisymmetric current develops small-scale breaking waves on each edge.

In each experiment the number n of waves that appeared around the annular current were counted.† This wavenumber increased linearly with $\mathscr{L}_0$ for each annulus. The wavelength was then calculated from $\lambda = 2\pi R/n$, where R is usually the mean radius of the annulus used. For 'wider' currents ($\mathscr{L}_0 > 2$), though, there was a smaller number of waves on the inner edge of the current than on the outer edge. However,

---

† Measurements of wavelength were always taken after the disappearance of any small-scale Kelvin–Helmholtz billows if the two length scales were distinctly separated.

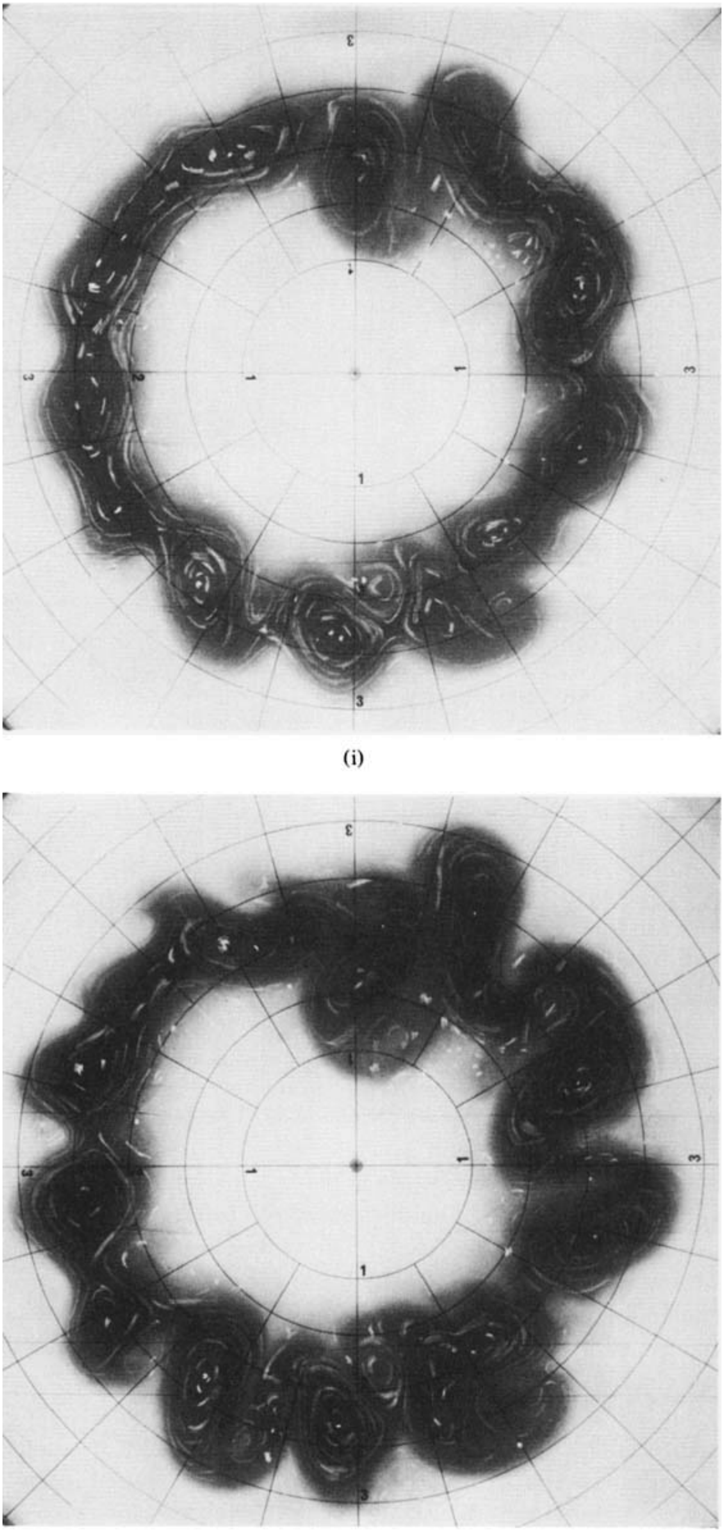

FIGURE 11. The evolution of a laboratory current with a shallow lower layer. $W_0 = 2{\cdot}0$ cm, $f = 1{\cdot}44\ \mathrm{s}^{-1}$, $\mathscr{L}_0 = 1{\cdot}07$ and the ratio of layer depths is 0·84. Times in number of revolutions after withdrawal of the annulus are (i) $t = 2$; (ii) 4.

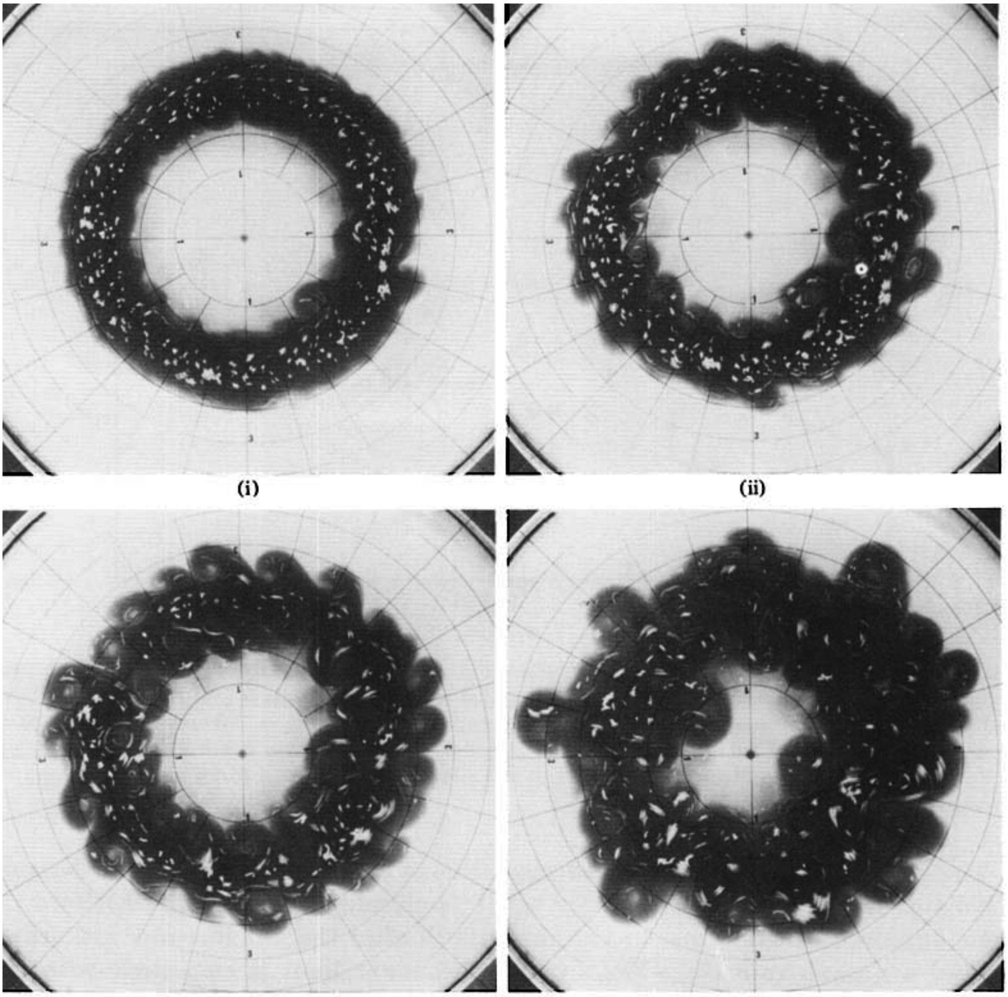

(i) (ii) (iii) (iv)

FIGURE 12. The evolution of a laboratory current with a shallow lower layer. $W_0 = 3{\cdot}9$ cm, $f = 1{\cdot}77\ \mathrm{s}^{-1}$, $\mathscr{L}_0 = 3{\cdot}7$ and the ratio of layer depths is 0·9. Times in number of revolutions after withdrawal of the annulus are (i) $t = 1$; (ii) 3; (iii) 5; (iv) 8.

using the appropriate radius of each edge after the initial collapse yielded two very similar wavelengths. A more serious problem at large $\mathscr{L}_0$ was that the wavelengths increased with time, and this may be due to a similarity of the scales of Kelvin–Helmholtz and rotationally dominated disturbances.

The dimensionless wavelength $f\lambda/(g'H_0)^{\frac{1}{2}}$ is plotted on figure 13, where the symbols indicate the annulus width and ratio of layer depths. Where the wavelength increased with time the two detectable extremes are plotted and connected by a vertical line. The computed wavelength $2\pi/k_{\mathrm{m}}$ (from figure 5*b*) is also plotted and the upper scale of the figure shows the current width L_0 after collapse as given by (6.2). For $\mathscr{L}_0 < 1$ ($L_0 < 2$) the observed wavelength increases slowly with $\mathscr{L}_0$ in roughly the same way as does the computed wavelength, but is almost a factor of two smaller. At $\mathscr{L}_0 > 2$ the observed instability has a roughly constant length scale, while the computed wavelength for the one-layer instability then increases rapidly with current width.

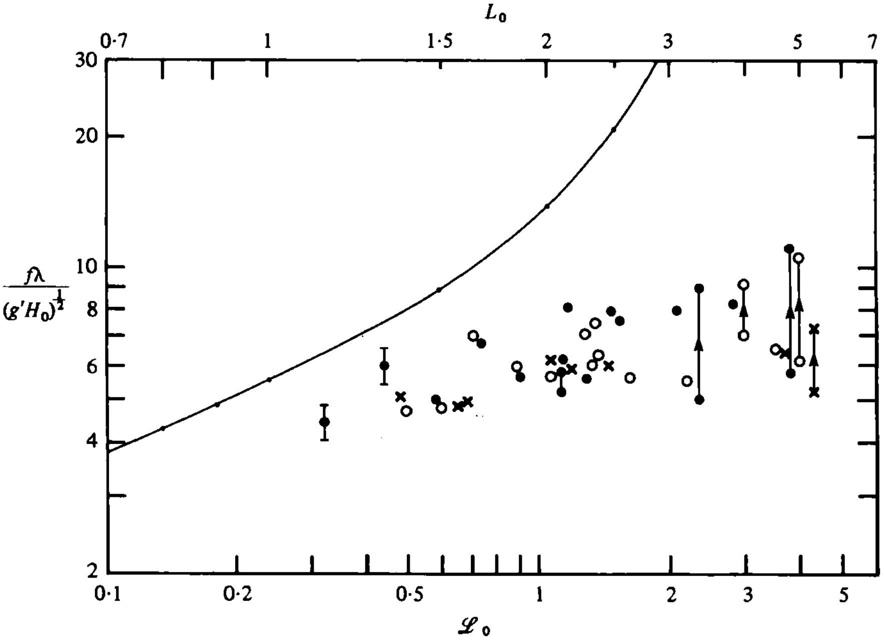

FIGURE 13. The observed dimensionless wavelength (based on the Rossby radius *before* geostrophic adjustment) as a function of the initial width of the current, $\mathscr{L}_0 = fW_0/(g'H_0)^{\frac{1}{2}}$. Data indicate the annulus used and the ratio of layer depths: ●, $W_0 = 2{\cdot}0$ cm and depth ratio $\lesssim 0{\cdot}2$; ○, $W_0 = 3{\cdot}5$ or $3{\cdot}9$ cm and depth ratio $\lesssim 0{\cdot}2$; ×, depth ratio 0·8–0·9. The upper scale is the width L_0 *after* geostrophic adjustment (calculated from $\mathscr{L}_0$ and (6.2)) and the computed wavelength $2\pi/k_m$ is plotted on this scale.

The growth rates of the observed disturbances are difficult to quantify because their appearance and growth at very small amplitude is poorly defined. However, their appearance within one to two revolutions after the annulus was withdrawn implies a growth rate $|kc| \sim O(4\times10^{-2})$. This lower limit is consistent with the computed growth rate on figure 5(*b*) for $\mathscr{L}_0 < 1$. A more clearly defined time scale, and one that is of importance in oceanographic observations, is the period required for the axisymmetric flow to break up into isolated eddies whose circulations have pinched off from their neighbours. For those experiments with layer-depth ratios less than 0·2 this time scale was always close to 5 or 6 rotation periods, but it was as small as three revolutions (at $\mathscr{L}_0 \simeq 1$) when the depth ratio was large.

Discussion of the experimental results

The data on figure 13 are presented again on figure 14, along with the computed wavelength $2\pi/\epsilon_m$ for the most rapidly growing mode described in § 5. However, this time the wavelengths are normalized by the Rossby radius based on the maximum depth H of the current *after* its collapse to geostrophic balance. This depth is calculated from (5.2) after finding the balanced width L_0 from (6.2), and assumes that the initially uniform potential vorticity remained after the collapse. To well within the scatter of the data, the measured wavelength λ is a constant multiple of the Rossby radius: $f\lambda/(g'H)^{\frac{1}{2}} = 7{\cdot}4 \pm 1{\cdot}2$.

For $\mathscr{L}_0 < 2$ we have already described the qualitative appearance of the growing

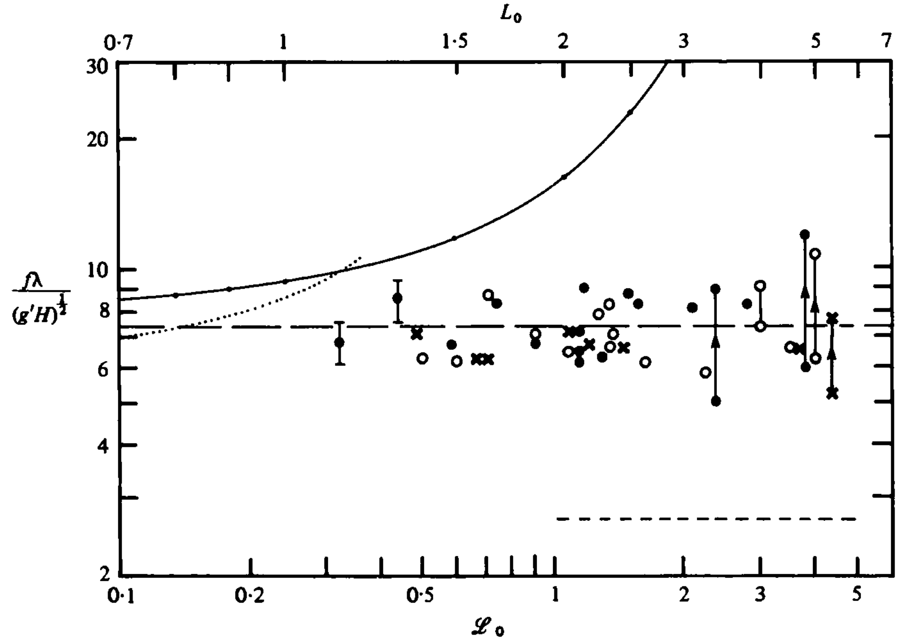

FIGURE 14. The data of figure 13 but with the wavelength renormalized using the calculated Rossby radius in the state of geostrophic balance (assuming conservation of potential vorticity). The data have a mean of $f\lambda/(g'H)^{\frac{1}{2}} = 7{\cdot}4 \pm 1{\cdot}3$ (broken line), which corresponds to the wavenumber $\epsilon = 0{\cdot}85 \pm 0{\cdot}15$. The computed wavelength $2\pi/\epsilon_m$ for the coupled mode on a current with uniform potential vorticity is also plotted (solid line). The dotted line shows the computed wavelength (against the upper scale) of the coupled mode with maximum growth rate for the profile (6.3), which has a varying potential vorticity. The dashed line is the computed wavelength of the mode attached to a single front for the same profile (6.3).

disturbances, and, for a sufficiently deep lower layer, this appears to be identical to that predicted for the one-layer instability. The two edges of the current couple together and give rise to both meandering and varicose structures which are $\frac{1}{2}\pi$ radians out of phase. The growing disturbances are stationary and large anticyclonic eddies develop from the wider and deeper sections of the wave. The computed and observed growth rates are also consistent with each other. On the other hand, no rapid change of growth rate with current width L_0 could be detected, and the measured wavelengths are smaller than those predicted. These discrepancies we attribute largely to the simultaneous instability of at least one other mode, a mode which becomes dominant only at larger current widths ($\mathscr{L}_0 > 2$), and which appears to have a length scale close to 2π deformation radii and growth rates of order 10^{-2}–10^{-1}. This mode is discussed below. There are also a number of other factors that may possibly influence the observed wavelength at $\mathscr{L}_0 < 1$. First, the formation of a 'narrow' current in our experiments requires that the upper layer have a large Rossby radius of deformation, which means that the collapse to geostrophic balance involves an extensive, rapid spreading of the buoyant fluid, leaving a rather shallow current. Both mixing by Kelvin–Helmholtz billows (which could be clearly seen in ciné films) and friction may then affect the vorticity and current depth throughout the width of the undisturbed flow. Alteration of the potential vorticity profile can in itself lead to only small changes in the most unstable wavelength at $L_0 < 1$, as the behaviour must then approach the same limit of zero potential vorticity. To illustrate this with a quantitative example we have chosen the convenient (but otherwise arbitrary) depth profile

$$\bar{h} = 1 - \frac{y^2}{L_0^2} \frac{\cosh y}{\cosh L_0}, \tag{6.3}$$

and computed the wavelength and growth rate of the most unstable mode that couples the two edges of the current. This wavelength is plotted on figure 14 (dotted line), while the dimensionless growth rate is somewhat greater than that found for the uniform potential vorticity profile ($kc_i = 0{\cdot}21$ at $L_0 = 1$).

Another result of the dissipation of vorticity during the collapsing phase is a small reduction of the current depth H. This would imply that we have underestimated the value of the observed dimensionless wavelength $f\lambda/(g'H)^{\frac{1}{2}}$ on figure 14 (and similarly overestimated the predicted wavelength on figure 13). Other factors that we have neglected are non-zero perturbation velocities in the finite lower layer and interfacial friction, both of which may have a direct influence upon the energy balance in the growing disturbances.

The two edges of the current are again strongly coupled when $\mathscr{L}_0 < 1$, and the ratio of layer depths is close to one. However, the structure of disturbances is different from that at small depth ratios, with the current showing less tendency to meander, and the growth rate is noticeably greater. In this case, the lower layer cannot be considered stationary, since its depth changes significantly during the collapse to geostrophic equilibrium. Conservation of potential vorticity implies that the fluid velocity in this layer is in the opposite direction to that in the upper layer, and this must be expected to influence the form of the coupling between the two density fronts.

At $\mathscr{L}_0 > 2$, with all the depth ratios used, the collapse to geostrophy has little influence upon the fluid near the centre line. Under these conditions we observe a clear qualitative difference in the instability. Each front is observed to behave independently and develop waves, which have a length scale determined by the Rossby radius. Furthermore, the growth rate of the coupled, one-layer instability at $\mathscr{L}_0 > 2$ is predicted to be more than an order of magnitude smaller than at $\mathscr{L}_0 = 1$,† while the length scale is predicted to increase exponentially with $\mathscr{L}_0$. Hence we conclude that another mode of instability is present for $\mathscr{L}_0 > 2$. However, we are uncertain of the nature of this second mode. There are two possibilities: it may be a mode in which the second layer and the lower boundary play an important role, or else it may be another unstable mode (other than the one discussed in this paper) that is described by the single-layer equations (2.15)–(2.17).

The particular solution to the perturbation equations (2.15)–(2.17) that is discussed in §§ 3, 4 and 5 has the leading-order phase velocity $c_0 = U$, and represents an unstable coupling of the two free streamlines. However, we find numerically that there can be other unstable solutions with larger wavenumbers than those for the coupled-front mode. Although these other modes are not yet fully understood, we do know that each is concentrated close to one of the free streamlines and, to be unstable, requires a non-zero gradient of potential vorticity. Since the laboratory currents do involve a

† The expression (4.26) shows that a decrease of the growth rate should be expected for any profile that becomes steadily flatter near the critical layer; the argument is not limited purely to constant-potential-vorticity profiles.

variation of potential vorticity near their edges (due to mixing and friction), the one-layer model might therefore be able to describe the observed mode of instability for wide currents as well as the coupled mode observed for narrow currents. For the particular profile (6.3), which was chosen as a relatively simple variation on the profile (5.3) and which has a varying potential vorticity, numerical solutions show that the wavelength of the new frontal mode with maximum growth rate is a constant multiple of the Rossby radius. This result is plotted on figure 14 (broken line), where the predicted wavelength can be seen to be much smaller than those observed. However, it may be that the preferred length scale is determined by the width of the region of large shear at the current edge. This in turn is determined, in the experiments, by the Rossby radius $(g'H_0)^{\frac{1}{2}}/f$, and by mixing. Before useful conclusions can be drawn it will be necessary to investigate further profiles numerically, and to find a method by which the potential-vorticity profile of a laboratory current can be determined to a sufficient accuracy. At present we can only approximate this profile by assuming conservation of potential vorticity during the collapse to geostrophic balance.

The observed mode of instability for wide currents may also require the presence of a lower layer of finite depth. On the basis of previous quasi-geostrophic theories, conditions at $L_0 > 1$ are well-suited to the appearance of a two-layer baroclinic instability. Since L^2 (after the initial collapse) is a Froude number of the flow, all the laboratory currents should be baroclinically unstable, and larger values of L_0 will give rise to baroclinic waves with larger growth rates. In experiments similar to those reported in this article, Griffiths & Linden (1981) have investigated unstable waves on an isolated two-layer vortex that is bounded by a sharp density front. They found that each growing wave led to the formation of a cyclone–anticyclone pair when the ratio of layer depths was greater than 10^{-1}. This behaviour is similar to that seen in figures 10 and 12, where disturbances grow independently on each edge of the wide currents, the lower layer plays a visible role, and a number of vortex pairs appear. Griffiths & Linden also detected a variation of wavelength with the ratio of layer depths. While no such dependence has been established conclusively for the length scales in the experiments reported here, the depth ratio does appear to influence significantly the value of the current width $\mathscr{L}_0$ at which the two-layer instability becomes dominant over the one-layer, coupled instability. This transition occurs at $\mathscr{L}_0 \simeq 2$ for depth ratios near 0·2, but at $\mathscr{L}_0 \simeq 1{\cdot}2$ for depth ratios near one. Griffiths & Linden also observed that when the layer depths are comparable, velocities within the cyclonic eddies, which extended throughout the depth of the lower layer, were comparable to those in the upper layer anticyclones. Hence the dynamical role of the second layer may well be important for the wide currents and at the large depth ratios in the present experiments.

7. Conclusions

A single-layer model of a gravity current that is bounded by two free streamlines on a uniformly sloping surface predicts that such a flow is unstable. The influence of vanishing layer depth and large inertial effects near the fronts are included. Normal modes are stable in the limit of infinitely large downstream length scales, but finite wavelengths are unstable. For currents that are symmetric about their midpoint, perturbations are simply advected with the mean velocity of the fluid. A combination of meandering and 'varicose' modes with a phase difference of $\frac{1}{2}\pi$ radians releases kinetic and potential energy from the basic current. When the flow has zero potential vorticity, the mode with maximum growth rate is predicted to have the wavelength $7{\cdot}9(g'H_0)^{\frac{1}{2}}f^{-1}$, where H is the maximum depth of the current, and an e-folding time of $(0{\cdot}14f)^{-1}$, or 0·57 rotation periods. Flows with finite (uniform) potential vorticity are characterized by the variable length scale $L_0 = fW/(g'H_0)^{\frac{1}{2}}$, where W is the half-width of the current and H_0 is a depth scale that characterizes the potential vorticity. The most rapidly growing mode in this case has a wavelength that increases with L_0 and a growth rate that decreases rapidly when $L_0 \gg 1$. Thus, in contrast to the well-known Rayleigh inflection theorem for quasi-geostrophic flows, we have demonstrated an instability that does not require an extremum (or even a gradient) of potential vorticity. It seems likely that the presence of significant inertial forces might similarly destabilize other geophysical flows.

A second type of unstable solution to the single-layer equations has also been found, but has not been discussed here. In this second mode of instability, perturbations are linked to one edge of the current, and require a non-zero potential vorticity gradient if they are to grow. As this mode may also be of geophysical significance (perhaps even in the case of a single isolated density front), it will be described in another paper.

Our laboratory experiments with a current at the free surface of a rather deep lower layer confirm that a current with two fronts (and nearly uniform potential vorticity) is unstable. The observed structure of growing disturbances, when the current width $L_0 < 3$, corresponds closely to that predicted. The velocity perturbations first form 'cat's-eye' structures at the centre line of the current, and the two edges co-operate to form eventually a train of large anticyclonic eddies. The experiments also indicate that the single-layer instability due to the coupling of the two free streamlines is likely to continue to be important when the lower layer is relatively shallow, providing that $L_0 < 2$.

A different mode of instability appears to make the dominant contribution to the release of energy from the laboratory currents when $L_0 > 3$. Each edge of the upper layer then behaves independently and the lower layer plays a visible role. However, because the observed non-dimensional wavelength is independent of the theoretical parameter (current width) over the full range of parameters used, an unambiguous comparison of the experimental observations with theoretical predictions remains somewhat unsatisfactory.

The flow configuration that we have considered is somewhat similar to that of the Denmark Strait overflow, in which large, energetic oscillations are detected. Smith (1976) presents an intensive discussion of the data for this flow, and finds that the horizontal components of velocity are in quadrature, and there is a distinct cross-stream component of perturbation heat flux which has a uniform sign but varies in magnitude across the stream. The disturbances are attributed to a two-layer baroclinic instability and compared with the predictions of a quasi-geostrophic model. However, the presence of velocity components in quadrature and a cross-stream phase lag in the cross-stream velocity of up to 90°, may also be consistent with instability due to a coupling of the two edges of the dense current. The only mitigating factor in this hypothesis is that the cross-stream heat flux in the one-layer model, by (4.30), varies as $\tilde{u}$, and therefore takes both signs across the stream. However, an asymmetric depth profile could well lead to a very small region of reverse $\tilde{u}$ near one edge, so that detection of this area might be difficult. Further knowledge of the mean vorticity distribution and the influence of bottom curvature is necessary if the two instabilities are to be compared.

R. W. G. and M. E. S. wish to thank the staff and participants of the 1980 Geophysical Fluid Dynamics summer programme at the Woods Hole Oceanographic Institution for providing a stimulating environment during the summer. A first set of experiments was carried out at W.H.O.I. and we thank Mr B. Frazel for his expert assistance. The work was completed while R. W. G. and P. D. K. were supported by grants from the U.K. Natural Environment Research Council. M. E. S. also acknowledges partial support from the U.S. Office of Naval Research.

Appendix A. A Rayleigh integral argument

The following alternative derivation of the leading term in the growth rate may be found a helpful complement to the matching technique used in § 4 and appendix B, in so far as the assumptions on the structure of the eigenfunctions are apparently less severe.

From (2.15)–(2.17) and (4.1) it follows that, correct to $O(\epsilon^2)$, ϕ satisfies

$$(\tilde{c}+\bar{h}_y)\,\phi_{yy}-\bar{h}_{yy}\phi_y-\tilde{c}\left(\frac{1+\bar{h}_{yy}}{\bar{h}}\right)\phi = O(\epsilon^2), \tag{A 1}$$

where $\tilde{c} = c-U$. This is similar to (4.11). Division by $(\tilde{c}+\bar{h}_y)^2$ and integration yields

$$\frac{\phi_y}{\tilde{c}+\bar{h}_y}-\frac{\phi_y(-L)}{\tilde{c}+\bar{h}_y(-L)}-\tilde{c}\int_{-L}^{y}\frac{1+\bar{h}_{\eta\eta}}{(\tilde{c}+\bar{h}_\eta)^2}\frac{\phi}{\bar{h}}\,d\eta = O(\epsilon^2). \tag{A 2}$$

Equation (A 2) is to be solved subject to

$$\phi(-L) = 0, \tag{A 3}$$

and a condition at $y = +L$. To obtain this, note that integration of (2.17) gives

$$c\int_{-L}^{L}\hat{h}\,dy = \int_{-L}^{L}dy\,(\hat{u}\bar{h}+\bar{u}\hat{h}), \tag{A 4}$$

or, after use of (2.16),

$$\tilde{c}\int_{-L}^{L}\hat{h}\,dy = -i\epsilon^2\int_{-L}^{L}dy\,\bar{h}(\bar{u}-c)\,\hat{v}, \tag{A 5}$$

and so

$$\tilde{c}\phi(L) = -i\epsilon^2\int_{-L}^{L}dy\,\bar{h}(\bar{u}-c)\,\hat{v}, \tag{A 6}$$

which is equivalent to (4.21).

It is readily seen that, when $\epsilon = 0$, a solution to (A 1), (A 3) and (A 6) is

$$\phi = \phi_0 \equiv \alpha\bar{h}, \quad c = U \quad (\text{or} \quad \tilde{c} = 0), \tag{A 7}$$

where α is an arbitrary amplitude factor. We shall now obtain an integral expression for the next term in c, i.e. $\tilde{c}$. By integrating (A 2) for ϕ, and using (A 7) for $\phi\bar{h}^{-1}$ in the integral, we obtain

$$\phi(y)-\frac{\phi_y(-L)}{\tilde{c}+\bar{h}_y(-L)}\left\{\bar{h}+\tilde{c}(y+L)+\tilde{c}\int_{-L}^{y}(\tilde{c}+\bar{h}_\eta)\,d\eta\int_{-L}^{\eta}\frac{1+\bar{h}_{\zeta\zeta}}{(\tilde{c}+\bar{h}_\zeta)^2}d\zeta\right\} \\ = O(\tilde{c}^2)+O(\epsilon^2), \tag{A 8}$$

where α is taken as $\phi_y(-L)\,(\tilde{c}+\bar{h}_y(-L))^{-1}$ for convenience. Substitution in condition (A 6) then gives

$$\tilde{c}^2\left\{2L+\lim_{\tilde{c}\to 0}\int_{-L}^{L}(\tilde{c}+\bar{h}_y)\,dy\int_{-L}^{y}\frac{1+\bar{h}_{\eta\eta}}{(\tilde{c}+\bar{h}_\eta)^2}\,d\eta\right\}=-\epsilon^2\int_{-L}^{L}dy\,\bar{h}\tilde{u}^2, \tag{A 9}$$

to leading order. Reversing the order of integration in (A 9) gives

$$\tilde{c}^2\left\{2L+\lim_{\tilde{c}\to 0}\int_{-L}^{L}\frac{1+\bar{h}_{yy}}{(\tilde{c}+\bar{h}_y)^2}\,[\tilde{c}(L-y)-\bar{h}]\,dy\right\}=-\epsilon^2\int_{-L}^{L}dy\,\bar{h}\tilde{u}^2. \tag{A 10}$$

The term in $\tilde{c}$ inside the integral is negligible, and by rearrangement we obtain

$$\tilde{c}^2\left\{2L-\lim_{\tilde{c}\to 0}\int_{-L}^{L}dy\,\frac{\bar{h}\bar{h}_{yy}}{(\tilde{c}+\bar{h}_y)^2}-\lim_{c\to 0}\int_{-L}^{L}\frac{\bar{h}\,dy}{(\tilde{c}+\bar{h}_y)^2}\right\}=-\epsilon^2\int_{-L}^{L}dy\,\bar{h}\tilde{u}^2. \tag{A 11}$$

It is readily shown that the first two terms inside the brackets combine to give a negligible term of order $\tilde{c}$. Thus

$$\tilde{c}^2=\frac{\epsilon^2\displaystyle\int_{-L}^{L}dy\,\bar{h}\tilde{u}^2}{\displaystyle\lim_{c\to 0}\int_{-L}^{L}\frac{\bar{h}\,dy}{(\tilde{c}+\bar{h}_y)^2}}. \tag{A 12}$$

The denominator in (A 12) can be written as

$$\int_{-L}^{L}\frac{\bar{h}\,dy}{(\tilde{c}+\bar{h}_y)^2}=\int_{-L}^{L}\frac{\bar{h}\,dy}{(\tilde{u}-\tilde{c})^2}=\left(\int_{-L}^{y_c-\delta}+\int_{y_c+\delta}^{L}\right)\frac{\bar{h}\,dy}{(\tilde{u}-\tilde{c})^2}+\int_{y_c-\delta}^{y_c+\delta}\frac{\bar{h}\,dy}{(\tilde{u}-\tilde{c})^2}, \tag{A 13}$$

where $\delta\to 0$, and y_c again represents (one of) the critical layer(s). For $\tilde{c}$ tending to zero, the right-hand side of (A 13) becomes

$$\begin{aligned}&\left(\int_{-L}^{y_c-\delta}+\int_{y_c+\delta}^{L}\right)\frac{\bar{h}\,dy}{\tilde{u}^2}+\int_{-\delta}^{\delta}\frac{[\bar{h}_c+O(\eta^2)]\,d\eta}{(\bar{u}_{yc}\eta+\frac{1}{2}\bar{u}_{yyc}\eta^2+\ldots-\tilde{c})^2}\\&\quad=\left(\int_{-L}^{y_c-\delta}+\int_{y_c+\delta}^{L}\right)\frac{\bar{h}\,dy}{\tilde{u}^2}+\frac{\bar{h}_c}{\bar{u}_{y_c}^2}\int_{-\delta}^{\delta}\frac{d\eta}{\left(\eta-\dfrac{\tilde{c}}{\bar{u}_{yc}}\right)^2}\left\{1-\frac{\bar{u}_{yyc}\eta^2}{\bar{u}_{yc}\left(\eta-\dfrac{\tilde{c}}{\bar{u}_{yc}}\right)}+\frac{O(\eta^3)}{\left(\eta-\dfrac{\tilde{c}}{\bar{u}_{yc}}\right)}+\ldots\right\}.\end{aligned} \tag{A 14}$$

Now as $\delta\to 0$, integrals of $\eta^r(\eta-\tilde{c}\bar{u}_{yc}^{-1})^{-r}$ tend to $2\delta\to 0$, plus correction terms of order $\tilde{c}$ which also are negligible. Hence

$$\lim_{\tilde{c}\to 0}\int_{-L}^{L}\frac{\bar{h}\,dy}{(\tilde{c}+\bar{h}_y)^2}=\left(\int_{-L}^{y_c-\delta}+\int_{y_c+\delta}^{L}\right)\frac{\bar{h}\,dy}{\tilde{u}^2}+\frac{\bar{h}_c}{\bar{u}_{yc}^2}\left\{-\frac{2}{\delta}-\frac{\bar{u}_{yyc}}{\bar{u}_{yc}}[\log\delta-\log(-\delta)]\right\} \tag{A 15}$$

$$=\mathrm{Fp}\int_{-L}^{L}\frac{\bar{h}\,dy}{\tilde{u}^2}-\frac{i\bar{u}_{yyc}\pi\bar{h}_c}{|\bar{u}_{yc}|^3}, \tag{A 16}$$

taking $\log(-\delta)=\log\delta-i\pi\,\mathrm{sgn}\,(\bar{u}_{yc})$ as before. Hence the result (4.26) for $\tilde{c}^2$ is recovered.

REFERENCES

Griffiths, R. W. 1980 In *Report of* 1980 *Summer Program in Geophysical Fluid Dynamics, The Woods Hole Oceanographic Institution* (ed. G. Veronis & K. Mellor). *Woods Hole Tech. Rep.* WHOI-80-53.

GRIFFITHS, R. W. & LINDEN, P. F. 1981 The stability of vortices in a rotating stratified fluid. *J. Fluid Mech.* **105**, 283–316.

MANN, C. R. 1969 Temperature and salinity characteristics of the Denmark Strait overflow. *Deep-Sea Res.* **16**, 125–137.

NORMAN, A. C. 1972 A system for the solution of initial and two-point boundary value problems. In *Proc. Ass. Comp. Mech.* (*25th Anniv. Conf., Boston*), pp. 826–834.

ORLANSKI, I. 1968 Instability of frontal waves. *J. Atmos. Sci.* **25**, 178–200.

PEDLOSKY, J. 1964 The stability of currents in the atmosphere and ocean. Part I. *J. Atmos. Sci.* **21**, 201–219.

SMITH, P. C. 1976 Baroclinic instability in the Denmark Strait overflow. *J. Phys. Oceanog.* **6**, 355–371.

WORTHINGTON, L. V. 1969 An attempt to measure the volume transport of Norwegian Sea overflow water through the Denmark Strait. *Deep-Sea Res.* **16**, 421–432.